



**HAL**  
open science

## **From the lithosphere to the lower mantle: An aqueous-rich metal-bearing growth environment to form type IIb blue diamonds**

Lucille Daver, Hélène Bureau, Églantine Boulard, Éloïse Gaillou, Pierre Cartigny, Daniele L Pinti, Oulfa Belhadj, Nicolas Guignot, Eddy Foy, Imène Estève, et al.

### ► To cite this version:

Lucille Daver, Hélène Bureau, Églantine Boulard, Éloïse Gaillou, Pierre Cartigny, et al.. From the lithosphere to the lower mantle: An aqueous-rich metal-bearing growth environment to form type IIb blue diamonds. *Chemical Geology*, 2022, 613, pp.121163. 10.1016/j.chemgeo.2022.121163 . hal-03839325

**HAL Id: hal-03839325**

**<https://hal.science/hal-03839325>**

Submitted on 26 Apr 2024

**HAL** is a multi-disciplinary open access archive for the deposit and dissemination of scientific research documents, whether they are published or not. The documents may come from teaching and research institutions in France or abroad, or from public or private research centers.

L'archive ouverte pluridisciplinaire **HAL**, est destinée au dépôt et à la diffusion de documents scientifiques de niveau recherche, publiés ou non, émanant des établissements d'enseignement et de recherche français ou étrangers, des laboratoires publics ou privés.

**From the lithosphere to the lower mantle: an aqueous-rich metal-bearing growth environment to form type IIb blue diamonds**

Lucille Daver<sup>1,2\*</sup>, Hélène Bureau<sup>1</sup>, Églantine Boulard<sup>1</sup>, Éloïse Gaillou<sup>3</sup>, Pierre Cartigny<sup>4</sup>, Daniele L. Pinti<sup>2</sup>, Oulfa Belhadj<sup>5</sup>, Nicolas Guignot<sup>6</sup>, Eddy Foy<sup>7</sup>, Imène Estève<sup>1</sup> and Benoit Baptiste<sup>1</sup>

<sup>1</sup> Institut de Minéralogie, de Physique des Matériaux et de Cosmochimie (IMPMC), Sorbonne Université, CNRS UMR 7590, 75252 Paris Cedex 05, France

<sup>2</sup> GEOTOP and Département des sciences de la Terre et de l'atmosphère, Université du Québec à Montréal, Montreal, QC, H3C 3P8, Canada

<sup>3</sup> MINES ParisTech, PSL Research University, Musée de Minéralogie, 75006 Paris, France

<sup>4</sup> Institut de Physique du Globe de Paris, Université de Paris, 75005 Paris, France

<sup>5</sup> Centre de recherche sur la conservation, Muséum National d'Histoire Naturelle, 75005 Paris, France

<sup>6</sup> Synchrotron Soleil, 91191 Gif-sur-Yvette, France

<sup>7</sup> Université Paris-Saclay, CEA, CNRS, NIMBE/LAPA, 91191, Gif-sur-Yvette, France

Corresponding author: Lucilledaver@hotmail.fr

Type IIb diamonds; blue diamonds; boron; nitrogen; mineral inclusions; aqueous fluids; Fe-Ni alloys; lithosphere.

**Abstract.** A study of five diamonds containing mineral and fluid inclusions, selected among forty-nine specimens from the Cullinan Mine, South Africa, was carried out to better document the origin and formation of N-absent B-poor (type IIb) diamonds. The combination of several in-situ non-destructive techniques was used to identify the mineralogy and the chemical composition of primary and secondary inclusions. These include breyite, larnite, graphite, Fe-Ni-Cu native metallic alloys, sulfides of the pyrrhotite group, Ni-rich oxide and potential hydrous ferric sulfates. A common and abundant hydrous fluid containing  $\text{H}_2\text{O} + \text{CH}_4$  was also identified. From the various observations, we suggest that these type IIb diamonds grew in an aqueous oxidized fluid reacting with a reduced mantle characterized by low oxygen fugacity. Remnant pressures recorded in primary breyite by Raman shifts and XRD measurements enabled the calculation of minimal entrapment pressures of inclusions using elastic geothermobarometry. Applying pressure corrections caused by elastic relaxation, minimum trapping pressures from 4.9 GPa to 5.6 GPa were calculated, suggesting lithospheric depths consistent with the occurrence of numerous graphite inclusions. The association of breyite and larnite, which is often considered as an indicator of sublithospheric origin, also occurs at pressures of 6 GPa or lower in a  $\text{H}_2\text{O}$ -rich and carbonate/Ca-rich environment. The B-poor and N-absent features of type IIb diamonds do not require the classic subduction-related model of their formation. Whereas high-pressure minerals would host boron in cold subducting slabs, slabs are also important carriers of nitrogen into the deep mantle, with this latter element mostly absent in these diamonds. In our alternative model, the mantle is proposed as an alternative source of boron, whereby metallic alloys or N speciation between fluid and melt would still prevent the incorporation of nitrogen, leading to the expression of the blue, boron-related and N-absent features of type IIb diamonds. The observed mineralogical assemblage neither proves sublithospheric origin nor does exclude lithospheric

depths of formation for these diamonds. Hence, we propose that type IIb diamonds form in a mantle continuum, from sublithospheric to lithospheric depths.

## 1. Introduction

The study of natural diamonds and their mineral/fluid inclusions provides unique constraints on the mineralogy of the Earth's mantle from 120 km to approximately 800 km depth, i.e., from the lithosphere down to the lower mantle (Harte, 2010; Shirey et al., 2019). Diamonds are also a unique sample from which to infer the nature of parent metasomatic C-O-H-N-S fluids or melts percolating through the mantle (e.g., Schrauder and Navon, 1994; Cartigny et al., 2014; Smit et al., 2016; Stachel et al., 2017).

In addition to the traditional classification based on their nitrogen and boron content, diamonds are also classified based on the mineralogy and geochemistry of their solid and fluid inclusions. Most diamonds are of lithospheric origin (above 300 km depth) and are believed to grow in C-O-H-N-S bearing fluids (see reference above). Lithospheric diamonds usually contain olivine, pyroxene, garnet, spinel and sulfides (e.g., Meyer, 1987; Stachel and Harris 2009) as typical mineral inclusions. Superdeep diamonds (formed at depths between 410 to 800 km) are rare and contain typically majorite garnet, ferropericlaase, Ca-perovskite and bridgmanite (e.g., Shirey et al., 2013). The nature and composition of the parent fluids of sublithospheric diamonds are more difficult to assess because the oxygen fugacity should be much lower at these depths (approximately FMQ-5; Frost and McCammon, 2008). It is suggested that C, H and O in metal-saturated regions of the deep mantle are buffered to reduced compositions, with C being either dissolved into metallic liquids or existing as CH<sub>4</sub>-rich fluids (e.g., Shirey et al., 2019).

Based on the traditional classification, blue diamonds are defined as type IIb, having almost no nitrogen, while the blue color results from the presence of boron ( $\leq 8$  ppm; Gaillou et al., 2012). Boron, which substitutes for carbon in the crystal lattice of diamonds (Chrenko, 1973), is a highly mobile element in aqueous fluids and exhibits incompatible behavior during partial

melting. It is concentrated in oceanic sediments (1-100 ppm), hydrothermally-altered oceanic crust (9-70 ppm), as well as serpentinite (10-90ppm) and is often considered to be an indicator of slab contribution to island-arc melts (e.g., De Hoog and Savov, 2018).

Type IIb blue diamonds are very rare, constituting only  $\leq 0.02\%$  of the diamonds extracted worldwide (King et al., 1998; Gaillou et al., 2012). They are found in a few kimberlites from South Africa (Cullinan Mine), Botswana (Orapa and Karowe) and – of uncertain origin – from alluvial deposits in India (Kollur Mine). They are very expensive on the diamond market and therefore not readily available for research, as demonstrated by the scarcity of published studies (King et al., 1998; Gaillou et al., 2012; Smith et al., 2018a and b). Recently, based on inclusions of majorite, jeffbenite and bridgmanite trapped in a series of type IIb diamonds, Smith et al. (2018a) proposed that blue diamonds are sublithospheric and originate within either the transition zone or the lower mantle, in relation to subduction settings. Here, a collection of forty-nine type IIb diamonds extracted from the Cullinan Mine (formerly Premier Mine), South Africa, was examined. Five of these diamonds contain single or multi-phased inclusions and thus they were the focus of this study. Among these, five inclusion-bearing diamonds were analyzed with a combination of non-destructive in-situ methods to preserve the gems and avoid loss of the inclusions, with the aim of identifying their parent fluids and their growth conditions. Further, this study addresses why these type IIb diamonds contain both no nitrogen and very little boron, and discusses the appropriateness of linking boron-bearing diamonds to boron-rich environments, such as subduction zones.

## **2. Materials and Methods**

## *2.1 Geological background and samples*

The Cullinan kimberlite is located in the Gauteng Province, 130 km north-east of Johannesburg, in the center of the Kaapvaal craton, one of the oldest fragments of continental lithosphere of Archean age (Fig. 1). The crystallization ages of the Kaapvaal crust range from 3.6 to 2.6 Ga, and its mantle root – made up of highly-depleted mantle peridotites of dunite/harzburgite composition (Viljoen et al., 2004) – is as old as 3.5 Ga (Moser et al., 2001). The region became a stable continental plate at 3.0 Ga (Moser et al., 2001) and successively underwent one of the oldest recognized episodes of plate subduction 2.93-2.88 Ga ago (Schmitz et al., 2004). The Kaapvaal craton was intruded by repeated injections of magma, which gave rise to the layered structure of the Bushveld Complex at 2.05 Ga, refertilizing the lithosphere by melt-related metasomatic processes. The Cullinan kimberlite emplaced through the ultramafic-to-mafic rocks of the Bushveld Complex (Allsopp et al., 1989) at  $1.18 \pm 0.30$  Ga (Scoates and Friedman, 2008). This deposit is well-known for its large, colorless diamonds, such as the largest gem-quality rough diamond ever found, the Cullinan (3106 carats rough crystal), as well as its blue diamonds, such as the Cullinan Dream (24.18 ct fancy blue cut from a 122.5-ct rough).

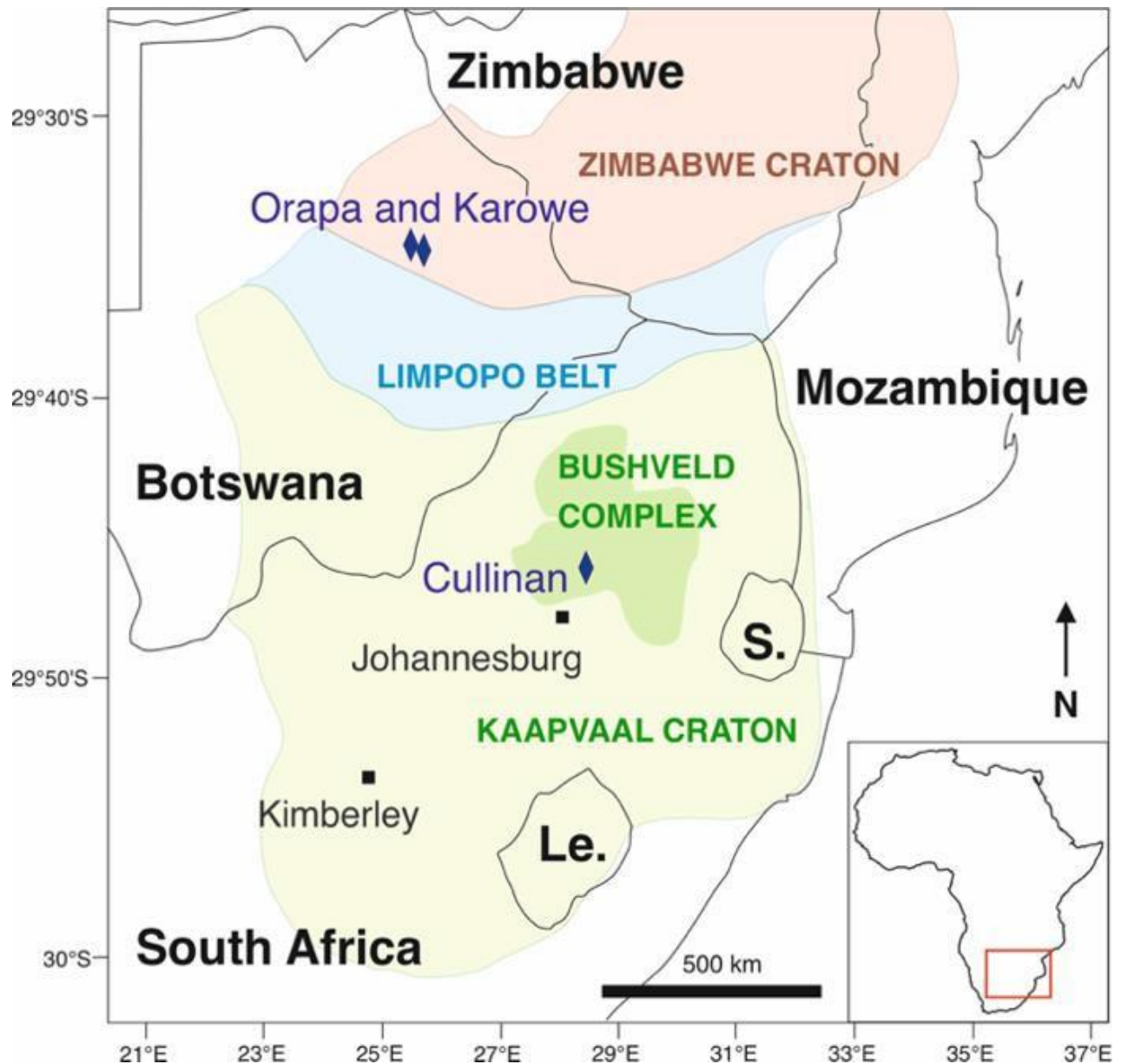


**Figure 1.** Simplified geological map of South Africa, with the Kaapvaal and the Zimbabwe cratons of Archean age. Blue diamond symbols indicate type IIb diamond mines. Abbreviations: Le.=Lesotho; S.=Swaziland.

Previous investigations revealed that most of the diamonds from the Cullinan Mine are of lithospheric origin (Deines et al., 1989; Thomassot et al., 2007), while Moore and Helmstaedt (2019) identified a bimodal population: 1) a Mg-rich suite (basic to ultrabasic, corresponding to sublithospheric diamonds; and 2) a Ca-rich suite (including breyite) linked to the websteritic suite and thus of lithospheric provenance. A few specimens are sublithospheric, as inferred from the



discovery of a perovskite-structured polymorph of  $\text{CaSiO}_3$  (Nestola et al., 2018). In a detailed study of inclusions trapped in exceptional gem diamonds from Letseng mine (Lesotho), Smith et al. (2016) proposed a model involving crystallization from a redox-sensitive metallic liquid phase in the deep mantle. These large gems, referred to as CLIPPIR (for Cullinan-Like, Inclusion-Poor, relatively Pure, Irregularly shaped and Resorbed), contain inclusions of solidified Fe-Ni-C-S melt, wrapped in a thin fluid layer of  $\text{CH}_4 \pm \text{H}_2$  that would involve a subduction-related formation under metal-saturated conditions.

In the present study, a set of forty-nine type IIb diamonds from the Cullinan Mine production were selected and donated when the mine was still owned by De Beers (Fig. 2). The forty-nine diamonds are broken fragments from larger original crystals, faint to fancy blue in color, ranging from 1.5 to 5 mm in longest dimension with a similar rounded, irregular appearance. Despite being fragments, the presence of cleaved surfaces, conchoidal to irregular fractures and growth marks on thirty-two of the forty-nine specimens allowed in-situ measurements such as micro-FTIR, which revealed measurable amounts of uncompensated boron, confirming their type IIb nature. The irregular and rough surfaces of the remaining seventeen specimens made measurement of their boron content impossible. The detailed description of the totality of specimens is reported in Table 1.

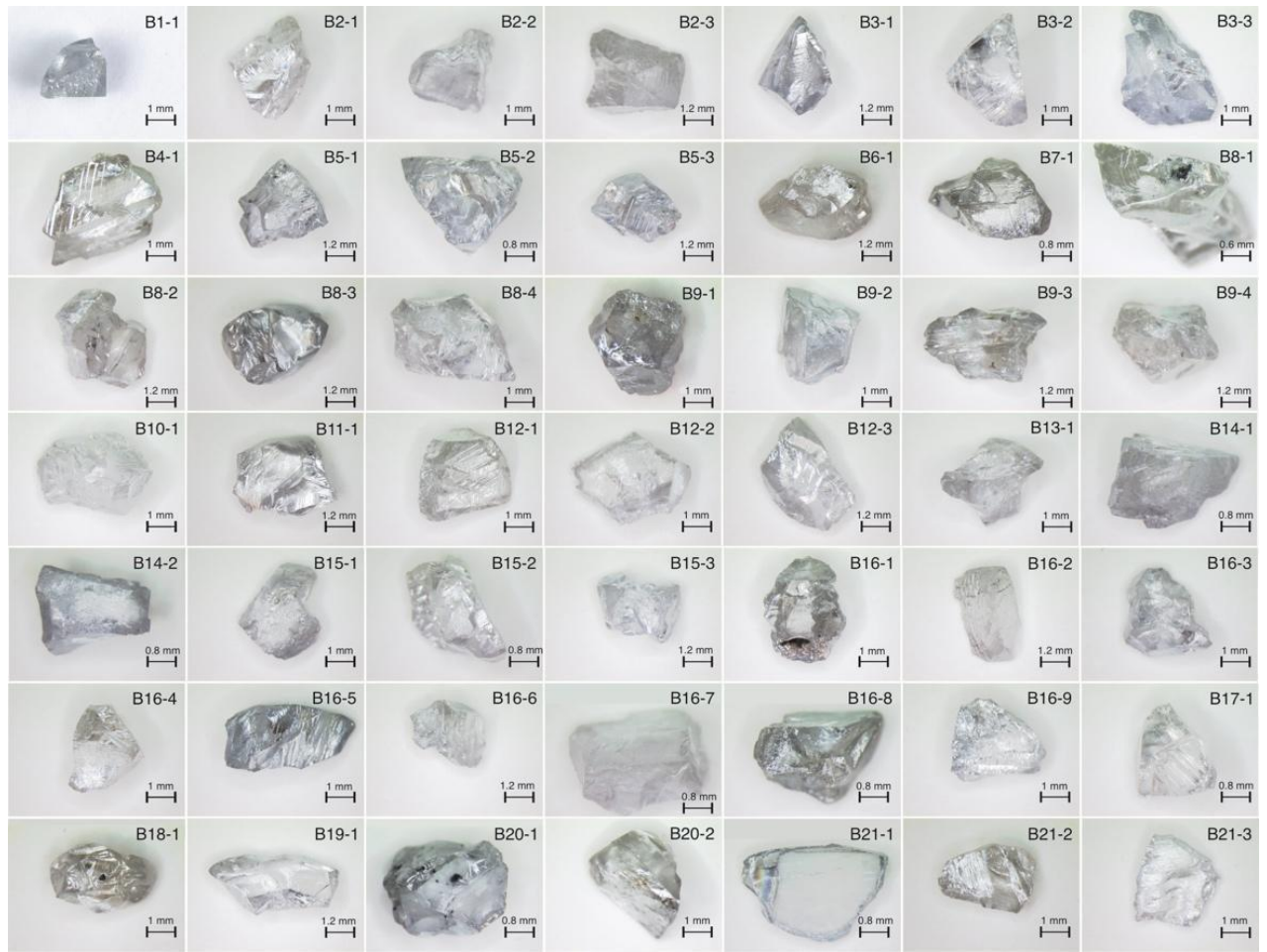


**Figure 2.** Photographs of the forty-nine type IIb diamonds donated by De Beers group from the Cullinan Mine.

**Table 1.** Summary of the FTIR, micro-Raman and SXRD measurements as well as inclusion descriptions of the studied type

IIb diamonds.

Name	Weight (ct)	Size (mm)	Description	Inclusion type	FTIR (B ppm)	Raman <sup>1</sup>	SXRD	XRF	SEM-EDX
B1-1	0.27		Fancy light blue crystal with an irregular shape and a fracture	None	NM	nm	nm	nm	nm
B2-1		2.5 × 2.5	Faint blue crystal with an irregular shape and conchoidal fractures	None	NM	nm	nm	nm	nm
B2-2	0.52	2.5 × 2	Faint blue crystal with an irregular shape	None	NM	nm	nm	nm	nm
B2-3		3.6 × 2.4	Faint blue crystal with an irregular shape and growth marks on the surface	None	NM	nm	nm	nm	nm
B3-1		4.2 × 2.4	Light blue crystal with an irregular shape and growth marks on the surface	Primary: black, flat dendritic inclusions	NM	NM <sup>2</sup>	nm	nm	nm
B3-2	0.40	4.8 × 3.12	Light blue crystal with an irregular shape and several cleaved surfaces	None	0.08	nm	nm	nm	nm
B3-3		3 × 3	Fancy light blue crystal with an irregular shape, a cleaved surface and iridescent colors in a fracture	None	0.61	nm	nm	nm	nm
B4-1	0.23	4 × 2	Faint blue macle, growth marks on the surface and iridescent colors in a fracture	Primary: small black inclusion	0.29	nm	nm	nm	nm
B5-1	0.60	2.4 × 3.48	Fancy light blue crystal with an irregular shape	Primary and Secondary: small black inclusions close to the surface	NM	NM	nm	nm	nm
B5-2		3.2 × 2.4	Fancy light blue crystal with an irregular shape and a cleaved surface	Primary: small black inclusions	NM	nm	nm	nm	nm

irregular shape and a cleaved surface

B5-3	3.24 × 2.4	Fancy light blue macle, growth marks on the surface and broken surfaces	None	0.29	nm	nm	nm	nm
B6-1	0.28 3.2 × 1.6	Faint blue crystal with an irregular shape, conchoidal fractures and iridescent colors in a fracture	Primary: black and colorless inclusions	NM	Graphite, breyite, larnite	nm	Fe-Ni-Cu alloy	nm
B7-1	0.26 2.96 × 2	Faint blue crystal with an irregular shape, growth marks on the surface and conchoidal fractures	None	0.39	nm	nm	nm	nm
B8-1	1.5 × 2.4	Light blue crystal with an irregular shape, a cleaved surface and growth marks on the surface	Primary and Secondary: cubo-octahedral shaped mineral inside a circular inclusion in healed fractures, and black inclusions	0.22	Graphite, H <sub>2</sub> O, methane	Graphite, <i>fcc</i> -(Ni,Fe), <i>bcc</i> -(Fe,Ni),	Fe-Ni alloy	nm
B8-2	0.93 2.04 × 3.6	Light blue crystal with an irregular shape, and a cleaved surface	Primary: black inclusions	0.23	Graphite	nm	nm	nm
B8-3	4.2 × 3	Light blue-gray crystal with an irregular shape	Primary: small black inclusions	0.35	NM	nm	nm	nm
B8-4	4.5 × 3	Faint blue crystal with an irregular shape and a cleaved surface	None	0.23	nm	nm	nm	nm
B9-1	3 × 3	Light blue-gray crystal with an irregular shape and growth marks on the surface	Primary: small black inclusions	0.23	NM	nm	nm	nm
B9-2	0.73 3 × 2	Fancy light blue macle, several cleaved surfaces and growth marks on the surface	Primary: small black inclusions	NM	nm	nm	nm	nm
B9-3	3.6 × 2.4	Faint blue crystal with an irregular shape and growth marks on the surface	Primary: small black inclusions	0.12	nm	nm	nm	nm
B9-4	2.4 × 3.6	Faint blue crystal with an irregular shape and growth marks on the surface	Primary: small black inclusions	0.34	nm	nm	nm	nm
B10-	0.20 4 × 2	Faint blue crystal with an irregular	None	NM	nm	nm	nm	nm

1			shape and growth marks on the surface						
B11-1	0.22	4.2 × 2.4	Faint blue-gray crystal with an irregular shape and growth marks on the surface	Primary: small black inclusions	0.17	NM	nm	nm	nm
B12-1	0.37	2.3 × 2.2	Faint blue crystal with an irregular shape and growth marks on the surface	Primary: small black inclusions	0.29	nm	nm	nm	nm
B12-2		2.7 × 4	Faint blue crystal with an irregular shape, growth marks on the surface and iridescent colors in a fracture	None	0.13	nm	nm	nm	nm
B12-3		4.2 × 2.4	Fancy light blue crystal with an irregular shape	Primary: small black inclusions	0.24	nm	nm	nm	nm
B13-1	0.12	3.5 × 1.5	Fancy light blue crystal with an irregular shape	Primary: small black inclusions	NM	nm	nm	nm	nm
B14-1	0.20	3.2 × 2.16	Fancy light blue crystal with an irregular shape	None	0.28	nm	nm	nm	nm
B14-2		3.6 × 1.6	Fancy blue crystal with an irregular shape	None	0.43	nm	nm	nm	nm
B15-1		3 × 3.2	Fancy light blue crystal with an irregular shape	None	NM	nm	nm	nm	nm
B15-2	0.36	1.2 × 3.6	Faint blue crystal with an irregular shape and growth marks on the surface	None	NM	nm	nm	nm	nm
B15-3		3.6 × 2.4	Fancy light blue crystal with an irregular shape	None	0.32	nm	nm	nm	nm
B16-1	1.10	4 × 3	Fancy blue crystal with an irregular shape, a cleaved surface, growth marks on the surface and iridescent colors in a fracture	Primary: black inclusions and Secondary: black cubo-octahedral shaped mineral inside a circular inclusion in healed fractures	0.38	Graphite, H <sub>2</sub> O, methane	Graphite, (Fe,Ni)O	Fe-Ni-Cu alloy	NiO, (Ni,Fe) alloys, pyrrhotite
B16-		4.44 ×	Faint blue crystal with an irregular	Primary: small black inclusions	NM	NM	nm		nm

2	2.4		shape and a cleaved surface								
B16-3	3 × 2.4		Fancy blue crystal with an irregular shape	irregular	None		NM	NM			
B16-4	3.2 × 2.8		Faint blue crystal with an irregular shape	irregular	None		0.19	nm	nm	nm	
B16-5	5 × 2.5		Fancy blue crystal with an irregular shape and a cleaved surface	irregular	Primary: small black inclusions		0.54	nm	nm	nm	
B16-6	3.6 × 2.4		Light fancy blue crystal with an irregular shape	with an irregular	None		NM				
B16-7	3.52 × 4.2		Light fancy blue crystal with an irregular shape and iridescent colors in a fracture		None		0.08	nm	nm	nm	
B16-8	4 × 1.6		Fancy blue-gray crystal with an irregular shape and a cleaved surface		None		NM				
B16-9	3 × 3		Light fancy blue crystal with an irregular shape and iridescent colors in a fracture		None		0.30	nm	nm	nm	
B17-1	0.07	2.88 × 2.4	Faint blue crystal with an irregular shape and growth marks on the surface	irregular	None		0.04	nm	nm	nm	
B18-1	0.13	2.7 × 4	Faint blue-gray crystal with an irregular shape and growth marks on the surface	with an irregular	Primary: black inclusions		NM	Graphite, H <sub>2</sub> O, methane	nm	nm	
B19-1	0.17	5.64 × 2.4	Faint blue-gray crystal with an irregular shape and a cleaved surface	with an irregular	None		0.32	nm	nm	nm	
B20-1	0.31	2.4 × 3.36	Fancy blue crystal with an irregular shape and conchoidal fractures	irregular	Primary: small and large black inclusions		0.31	Graphite, O-H, breyite, lamite, ferricopiapite	Graphite, breyite, <i>bcc</i> -(Fe,Ni), <i>fcc</i> -(Ni,Fe)	Fe-Ni-Cu alloy	nm

B20-2	2 × 3.5	Light fancy blue-gray crystal with an irregular shape and a cleaved surface	Primary: small black inclusions	NM	NM	nm	nm	nm
B21-1	4.56 × 2.96	Light fancy blue crystal with a flat shape, a cleaved surface and iridescent colors in a fracture	Primary: small black inclusions	0.19	NM	nm	nm	nm
B21-2	0.22 2.5 × 3.6	Light fancy blue-gray crystal with an irregular shape and growth marks	Primary and inclusions	Secondary: small black 0.09	NM	nm	nm	nm
B21-3	3.2 × 3.1	Light fancy blue crystal with an irregular shape and a cleaved surface	None	0.25	nm	nm	nm	nm
<hr/> 1: measured if contains inclusions; NM: not measurable in situ; nm: not measured								

Twenty-four of the forty-nine diamonds display either single phase or multiple phase inclusions, including both solids and fluids. Among them, five diamonds (samples B6-1, B8-1, B16-1, B18-1 and B20-1) exhibit measurable inclusions with non-destructive techniques such as FTIR and micro-Raman spectroscopy (Fig. 3). These five samples were studied in situ, to prevent any irreversible damage on the inclusions, except for specimen B16-1 which had been selected to expose a part of its inclusions.

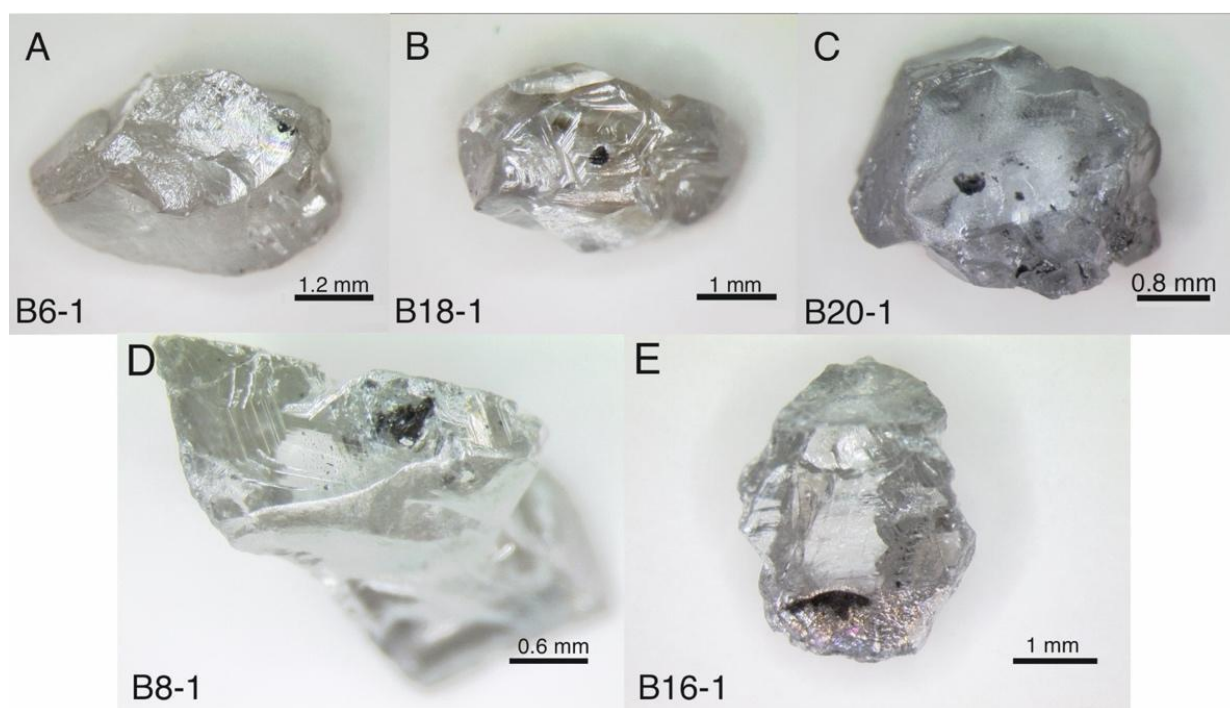


**Figure 3.** Photographs of the five type IIb diamonds containing multi-phased mineral inclusions selected for this study: (A) sample B6-1, (B) sample B18-1, (C) sample B20-1, (D) sample B8-1 and (E) sample B16-1.

## 2.2 Methods

### 2.2.1 Cryo ion-beam milling

To obtain one mirror-polished section and to preserve the inclusions from tearing, sample B16-1 was exposed using ionic argon cryo-polishing, performed under high vacuum and at -



100°C. A Leica EM TIC 3X Ion Beam Milling System device was used, which allows perfect polishing using three broad argon ion beams. The three ion beams intersect at the edge of a tungsten carbide mask, which partially hides the sample. The area of the sample that is exposed to the beams (100µm from the edge) was sputtered at 10kV, 3.5mA. The diamond milling rate is almost 10 times lower than the Si milling rate at 10 kV (300µm/h with Ar<sup>+</sup>).

### 2.2.2 Micro-FTIR spectroscopy

To determine the uncompensated boron concentration, Fourier Transform InfraRed (FTIR) spectroscopy measurements were performed on the forty-nine specimens (Table 1; Fig. 4). A Bruker IFS 66v/s FTIR spectrometer, equipped with a continuum infrared microscope with a 32 × transmission/reflection objective and an aperture of 250 × 250 µm, was used at the *Institut de Minéralogie, de Physique des Matériaux et de Cosmochimie* (IMPMC), Sorbonne Université. Absorbance was measured at the maximum light transmission for 72 s over a spectral range of 600 to 6000 cm<sup>-1</sup> and a spectral resolution of 4 cm<sup>-1</sup>, with 128 scans accumulated for each spectrum. Background spectra were collected for 72 s before analyses and are subtracted from each measured absorbance spectrum. Diamond spectra were normalized to 12.2 Au (absorbance units) at 1994 cm<sup>-1</sup> wavenumbers to convert from absorbance to absorption coefficient values (Collins, 1982). Boron concentration was determined in thirty-two of the forty-nine samples (Table 1) at 2800 cm<sup>-1</sup> using an absorption coefficient of 0.035 ppm cm<sup>-1</sup> to obtain the uncompensated boron content in atomic ppm (Fisher et al., 2009).

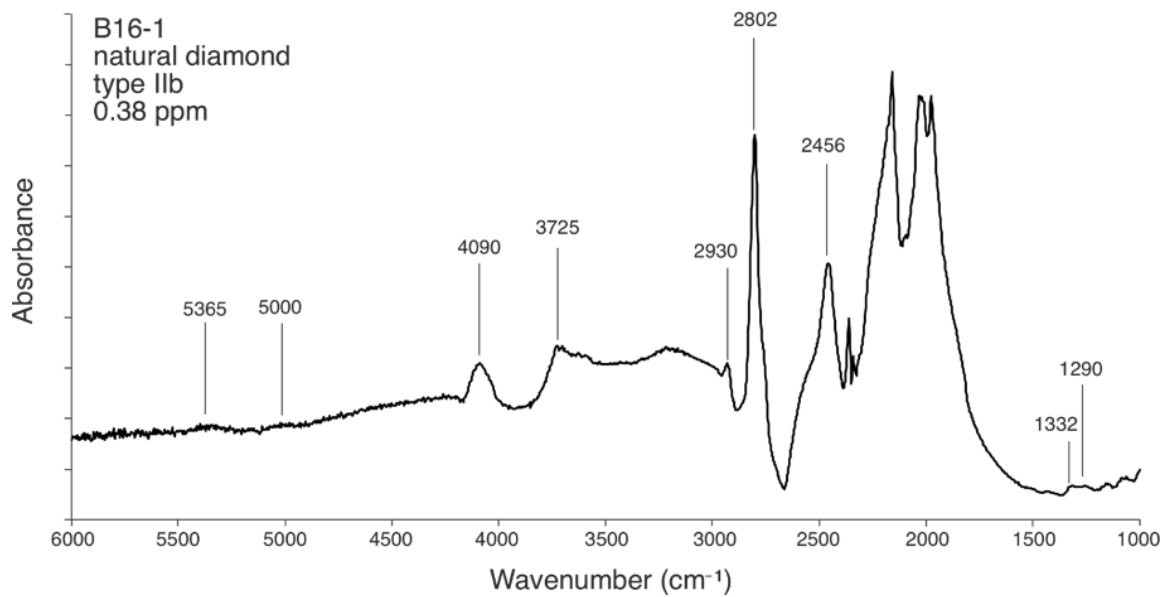


**Figure 4.** FTIR spectra of sample B16-1. Typical boron-related bands are labeled on the spectrum with their wavelength values. The boron concentration of 0.38 ppm is calculated using FTIR spectra normalization at 1994  $\text{cm}^{-1}$ , with  $y = 12.2 \text{ Au}$  (absorbance/cm).

### 2.2.3 Micro-Raman spectroscopy

Confocal micro-Raman spectroscopy measurements were performed in situ on all accessible inclusions trapped in the diamonds to identify their nature. The samples were analyzed using a micro-Raman Invia Renishaw spectrometer at the *Centre de Recherche sur la Conservation of the Muséum National d'Histoire Naturelle*, Paris. A 532 nm wavelength excitation laser beam of a 2  $\mu\text{m}$  size was used for inclusion characterization, with scales ranging between 900  $\text{cm}^{-1}$  and 3600  $\text{cm}^{-1}$  at a power of less than 10% (corresponding to 8.5 mW on the sample at a magnification of 20  $\times$ ) to avoid any damage to the inclusions. Additionally, spectra were baseline corrected. Micro-Raman spectral imaging was performed on one inclusion with a high power of 50% (8.5 mW) on large areas of 20  $\times$  20  $\mu\text{m}$ .

### 2.2.4 Scanning electron microscopy

Scanning electron microscopy was performed at the IMPMC using a SEM-FEG Zeiss electron microscope. Imagery was performed on two bulk specimens (B16-1 and B8-1) using a voltage of 2 kV. Quantitative chemical analyses at the surface of the polished section of diamond B16-1 were obtained by energy dispersive X-ray (EDX) analysis, with a voltage of 15 kV using international standards (Astimex Standards Ltd.) as calibrants.

### 2.2.5 X-ray diffraction

X-ray diffraction (XRD) patterns were collected in situ on inclusions trapped in diamonds using the micro X-ray diffractometer installed at the *Pression Structure Imagerie par Contraste à Haute Énergie* (PSICHÉ) beamline of the SOLEIL synchrotron facility in Saclay, France. A monochromatic (33 keV) micro-focused beam ( $15 \times 20 \mu\text{m}$  VxH) was used. Inclusion-bearing diamonds were fixed on copper pinholes to facilitate pre-alignment in the X-ray beam. The inclusions were then optically-aligned on the vertical rotation axis of the goniometer using the high-resolution objectives available on the beamline. Diamond refraction was further minimized by selecting only those inclusions very close to the surface (46 inclusions). This protocol allowed for the collection of data on large angle ranges ( $\pm 20^\circ$ ), both improving statistics while minimizing the effect of phase-preferential orientation inside the inclusions. Complementary in-situ XRD was performed at IMPMC, using a RIGAKU MM007HF Mo rotating anode X-ray diffractometer (17.48 KeV; wavelength of 0.7093 Å) equipped with Elliptical CMF/VariMax optics and a double image plate Raxis IV++ detector ( $300 \times 300 \text{ mm}$ ,  $1 \times 10^6:1$  photons/pixel,  $100 \times 100 \mu\text{m}$ ). This configuration allowed for a beam size of  $200 \mu\text{m}$  at the surface of the sample. Data analysis was performed using DIOPTAS software (Prescher and Prakapenka, 2015) to obtain 2D projections and GSAS software (Toby, 2001) to identify the phases.

### 2.2.6 X-ray fluorescence

X-ray fluorescence (XRF) analyses were carried out in situ on several dozen inclusions trapped close to the surface of the diamonds at the *Laboratoire Archéomatériaux et Préviation de l'Altération* of CEA-Saclay, France. A high-flux X-ray generator, equipped with a XENOCSS<sup>®</sup> FOX2D MO 25-25P multilayer mirror with a Mo source at 17.48 keV (Mo-Ka), was used to generate a monochromatic X-ray beam of  $30 \times 50 \mu\text{m}$ , with a flux of ca. 1 Mph/s. XRF spectra were collected through a Ketek AXAS Vitus Si-drift detector (SDD –  $10 \text{ mm}^2$  of active area) in reflection geometry. In-situ measurements of inclusions in the diamonds were monitored by a camera equipped with a focusing zoom. The strong absorption of fluorescence due to the thickness of the diamonds between the inclusions and the detector compromised the measurements of low-energy elements such as S, Si, K, Na and Ca, therefore allowing detection only above 6 KeV (i.e., Fe, Ni, Cu...). Semi-quantitative chemical analyses were carried out in situ on a few dozen inclusions trapped close to the surface of the diamonds.

## 3. Results

### 3.1 Boron contents

Boron concentration determined by FTIR spectroscopy ranged from 0.04 at.ppm to 0.61 at.ppm with a median value of 0.27 at.ppm (Table 1). It is worth remembering that only the uncompensated boron concentration (i.e., boron not compensated by another atom, usually nitrogen) can be measured using this method, which represents a lower limit for the real boron content in diamonds (Gaillou et al., 2012). As expected for type IIb diamonds, no nitrogen was detected by FTIR.

### *3.2. Mineralogical description of the inclusions*

#### *3.2.1. Primary inclusions*

Primary inclusions are defined as trapped during the growth of the host crystal (Roedder, 1979). These inclusions are therefore isolated inside the crystal, totally surrounded by the diamond without any connection to either the exterior or to another inclusion. They are therefore contemporaneous to or predate the formation of the diamond (i.e., syngenetic or protogenetic, respectively). Primary inclusions were found in B6-1, B16-1, B18-1 and B20-1 (Table 1). They occur as a single phase or as an association of multiple phases, forming isolated bodies, which are anhedral and more-or-less flat, possibly with a thin envelope of fluid-to-solid mixture (Fig. 5A, B and C). Their size varies from 20 to 500  $\mu\text{m}$  in diameter within the stones. These inclusions provide information about the growth environment, the parent fluids of the diamond and/or the synchronous solid/fluid phases present during its growth.

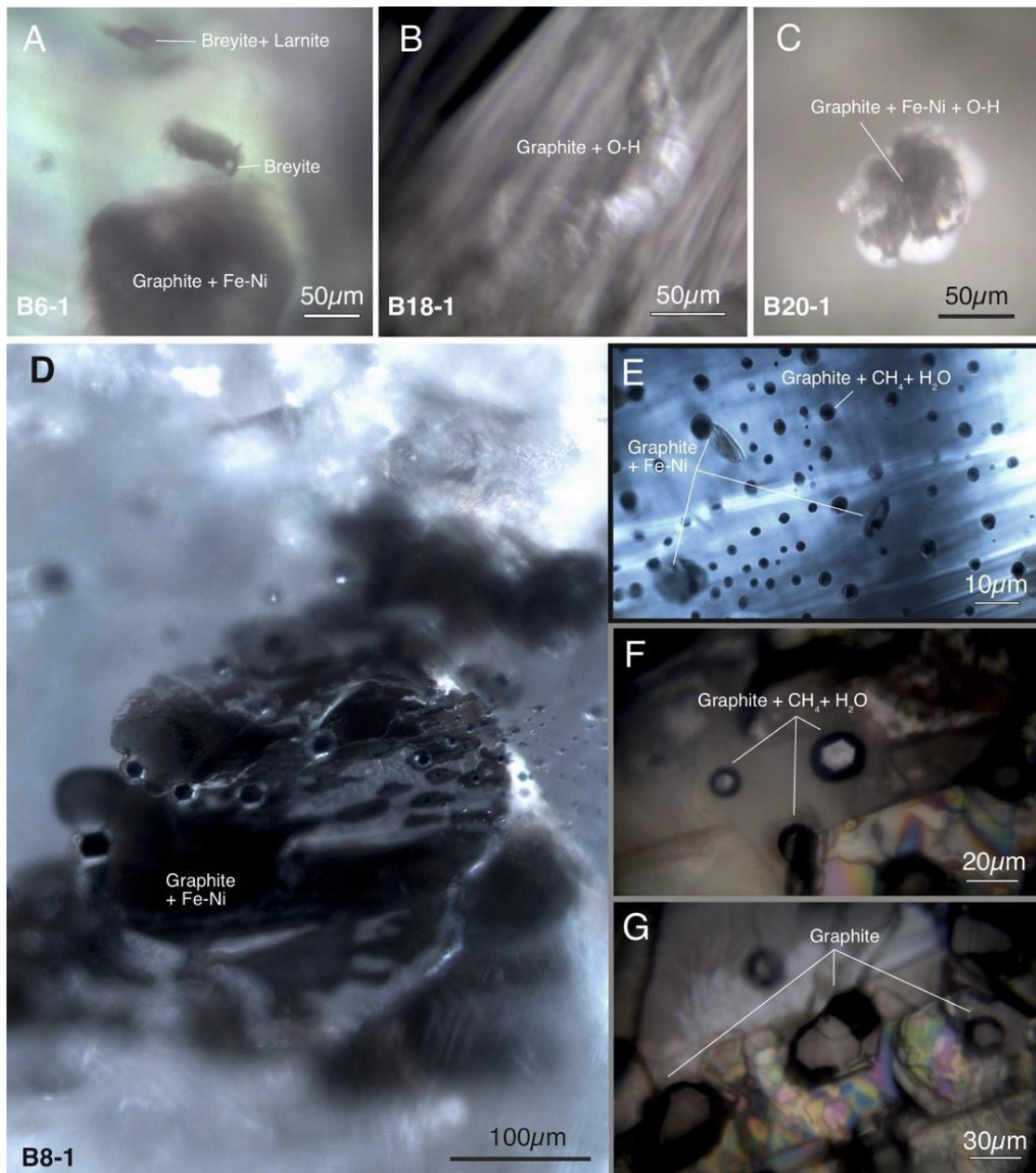


**Figure 5.** Images of inclusions in the studied diamonds. **A)** flat primary Fe-Ni-C inclusions in the center, small isolated breyite inclusions located at the bottom left and larnite and breyite inclusions at the top in sample B6-1. **B)** Primary graphite inclusion, surrounded by a fluid envelope in sample B18-1. **C)** Primary Fe-Ni and graphite inclusion, surrounded by a fluid envelope in sample B20-1. **D)** Secondary metallic cluster (Fe-Ni alloys and graphite) in a healed fracture in sample B8-1; small inclusions in front of the cluster are isolated graphite crystals surrounded by a fluid envelope. **E)** Larger view of the innermost part of the healed fracture in sample B8-1, which exhibits graphite crystals in the center, surrounded by a fluid envelope composed of water and methane (5-15  $\mu\text{m}$  in

size) and flat metallic Fe-Ni inclusions of various shapes and a gray hue. **F)** View of the same healed fracture, but closer to the fracture entrance; inclusions are  $\sim 20 \mu\text{m}$  in size with the same hexagonal graphite crystal in the center, surrounded by a fluid envelope. The healing of the fracture formed small cubo-octahedral-shaped diamonds, the grain boundaries of which connect the inclusions to each other. **G)** View of the same healed fracture at the fracture entrance. Inclusions exhibit the same graphite crystals (in gray) in the center, but their envelopes follow the morphology of the central graphite. They get larger, up to  $\sim 50 \mu\text{m}$ , and seem to be thicker. The cubo-octahedral diamond crystals healing the fracture are visible in the bottom part of the image, and display iridescent colors likely caused by optical density changes.

### 3.2.2. Secondary inclusions

The term “secondary inclusion” is defined as an inclusion trapped by the healing of fractures in the host crystal at some unspecified time after its growth (Roedder, 1979). Secondary inclusions are not isolated, occurring always in association with other inclusions, and postdate the trapping of the primary inclusions. Usually forming within a host crystal’s fractures, caused by fluid infiltration, secondary inclusions are possibly associated with protogenetic crystals and also manifest as inclusions aligned along lines or planes after the healing of fractures during a second stage of diamond growth (Fig. 5D). In our samples, they formed suites of inclusions, aligned along planes corresponding to the healing of the fractures by a second generation of diamond material and are associated with large dark inclusions (Figs. 5D-G and 6). This alignment is consistent with a fluid trapped along a crystalline plane.

Diamonds B8-1 and B16-1 exhibit similar secondary healed fractures. In both cases, the outer part of the fracture displays iridescence, though this does not extend to the innermost part of the fracture, indicating that the fracture is completely sealed from the exterior. These fractures are filled with multi-phased inclusions of various compositions and sizes: a mesh of small isolated inclusions (5 to 15  $\mu\text{m}$ ), whose sizes increase up to 50  $\mu\text{m}$  close to the edge of the

fracture, together with a few isolated small anhedral inclusions (Figs. 5E, F and G and 6); and large ( $> 300 \mu\text{m}$ ) clusters with a metallic aspect (Fig. 5D). In sample B8-1, three parallel healed fractures were observed, forming three layers of inclusions along cleavage planes (Fig. 6).

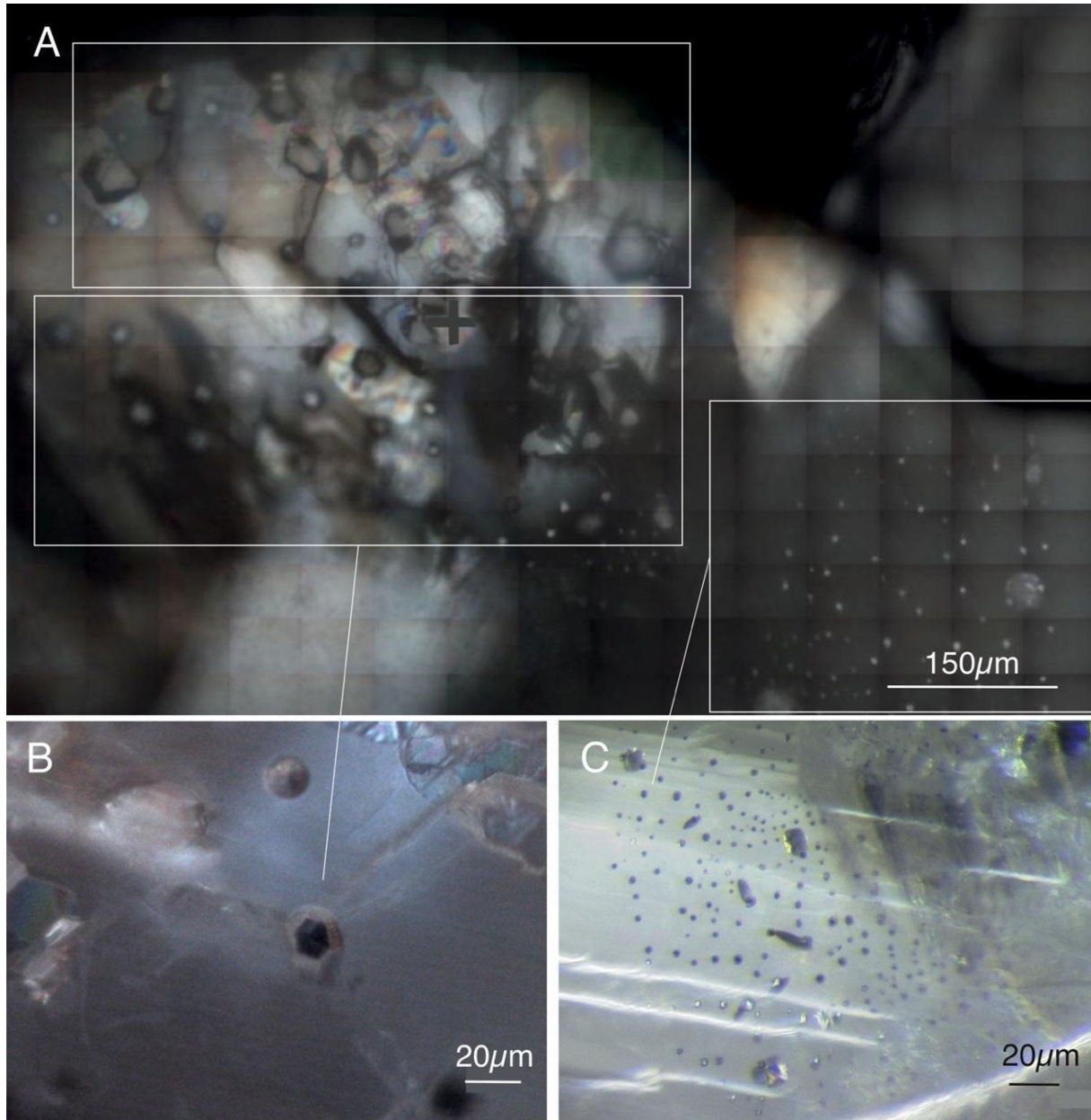


**Figure 6.** Images of secondary inclusions trapped in healed fractures of sample B8-1. A) Mosaic view of the entire healed fracture. From bottom to top, highlighted: a group of smaller multi-phased inclusions ( $5\text{-}10 \mu\text{m}$  size); a



*group of medium (15-20  $\mu\text{m}$ ) to large inclusions (30-50  $\mu\text{m}$ ) together in the middle of the healed fracture; a group of larger inclusions ( $\geq 50$   $\mu\text{m}$ ) at the end of the fracture. In the upper rectangle of this picture, central graphite crystals appear. B) Isolated inclusions observed mainly in the middle part of the fracture, formed within an envelope embedded with central graphite crystals. This morphology may be inherited from protogenetic graphite crystals trapped in the inclusions, the latter of which are connected by the grain boundaries between the diamond crystals that have healed the fracture. Some spherical, isolated graphite-free inclusions are also observed. C) View of the inner part of the fracture, composed of isolated inclusions from two populations: multi-phased with central graphite and metallic daughter crystals; and flat metallic inclusions of various shapes. No grain boundaries and no secondary diamond crystals were observed between the inclusions, suggesting the complete healing of the fracture.*

The healed fractures run from the edge of the crystal to  $\sim 1$  mm inside the crystal ( $1400 \times 800$   $\mu\text{m}$  for sample B8-1 and  $4500 \times 1800$   $\mu\text{m}$  for sample B16-1). Healed fractures exhibit distinct zonations from the core to the rim, with a cluster of small, isolated round and flat inclusions observed in the innermost part of the fracture, located in the core of the diamond, associated with shapeless metallic inclusions (Fig. 5E). The size of the inclusions progressively increases (from 5 to  $> 50$   $\mu\text{m}$ ) toward the surface (Figs. 5F, G and 6A), associated with a healing process which creates a mosaic of small diamond crystals mimicking the hexagonal shape of graphite. These crystals seem to be connected to each other, forming a network of grain boundaries (Figs. 5F, G and 6B).

Most of the isolated inclusions inside healed fractures show spherical to cubo-octahedral shapes, with the inclusions trapping hexagonal graphite crystals within the fracture (e.g., Fig. 6B). Their sizes range from 5 to 15  $\mu\text{m}$  in diameter in the inner part of the healed fracture, where they are isolated from each other (Figs. 5E and 6C), to  $< 50$   $\mu\text{m}$  in diameter at the limit of the fracture, where they are all connected with the grain boundaries of a small cubo-octahedral shaped diamond network (Fig. 5G). The geometry of the healed fractures and their various inclusions are illustrated in Figs. 5D, G and 6. Inclusions of Fe-Ni alloys and carbon (Fig. 5C-D)

have previously been observed in fractures of diamonds with similar appearance (Smith et al., 2017; Shatsky et al., 2020). However, it is worth noting that, here, no carbides were identified in our samples, with graphite being the main C-bearing phase found in the inclusions instead (Fig. 5C-D).

SEM imaging of the surface of diamonds B8-1 and B16-1 revealed that both diamonds have been fractured and healed (Figs. 7A, B). The composite inclusions (central crystal + envelope) exhibit cubo-octahedral shapes (Figs. 7A, C) and are connected with each other through new diamond crystal grain boundaries. Diamond B8-1 ( $3 \times 2 \times 1$  mm size) displays growth marks on its surface made of several triangular and six-sided pits on the fracture plane, indicating occurrence of minor resorption of the crystal. Diamond B16-1 ( $3 \times 2 \times 1$  mm size), by contrast, displays a resorbed surface with no visible growth marks. In this case, the euhedral cubo-octahedral shape of the graphite crystals trapped in the so-called secondary inclusions (Fig. 7A) would be more fittingly described as syngenetic (Glennemann et al., 2003), i.e., trapped together with the fluid rather than formed after the closure of the inclusion, with their shape therefore imposed by the diamond. It is worth noting that diamond B16-1 contains both primary and secondary inclusions crystallized in a subsequent generation of diamond, from which at least two growth episodes can be inferred.

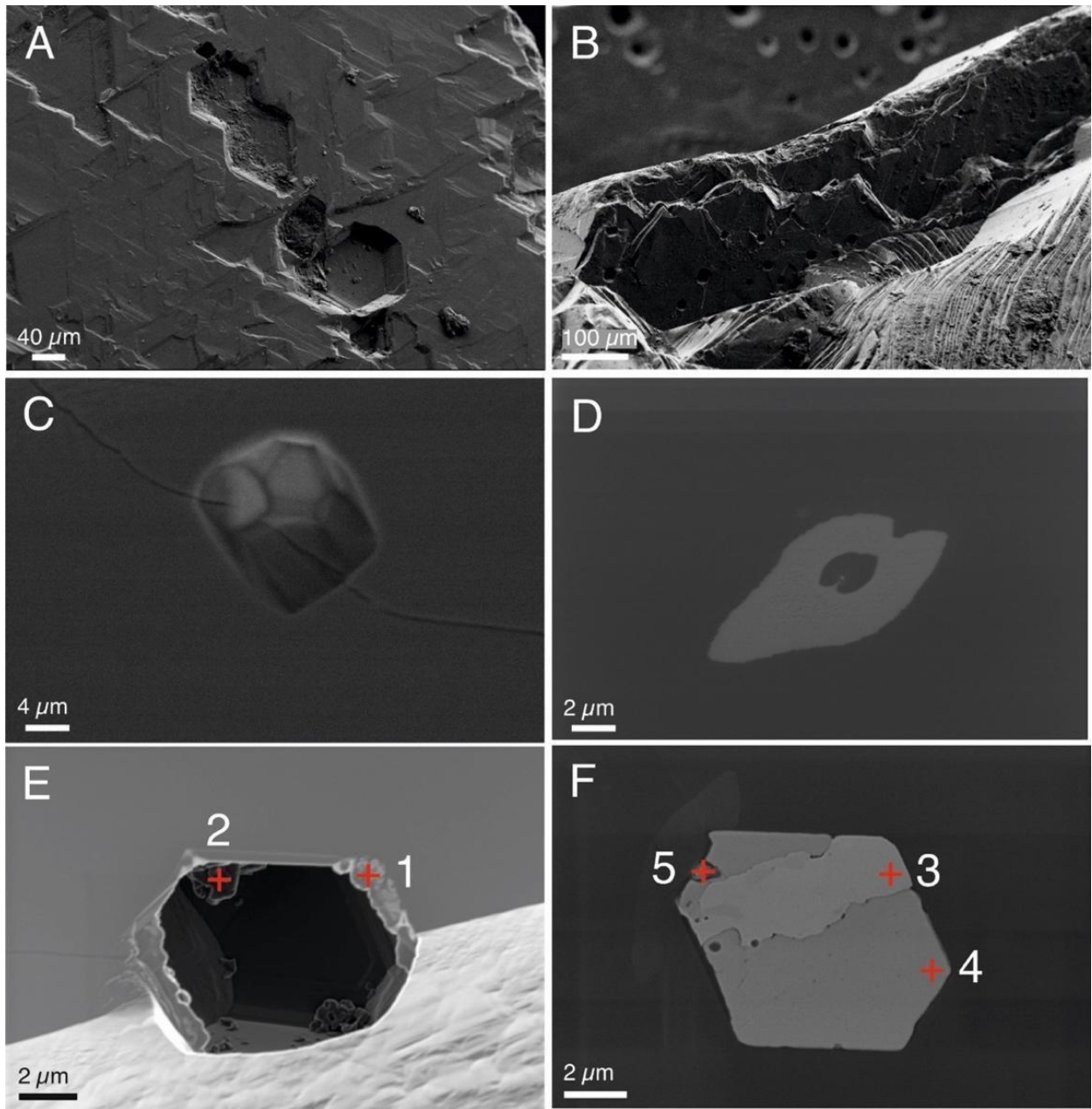


**Figure 7.** SEM images of secondary inclusions in diamonds B8-1 and B16-1. A to B: at the diamonds' surfaces (left to right: B8-1 & B16-1), where healed fractures are visible; C to F: diamond B16-1 after experiencing cryo-ionic polishing perpendicular to the fracture. A) The surface of sample B8-1 exhibits triangular and six-sided pits, which correspond to the prints of the now-empty fluid inclusions. B) As with B8-1, sample B16-1's surface displays a resorbed texture. C) Close-up of one inclusion, just below the surface, that is still closed in sample B16-1. A few smaller crystals in the fluid have been observed. D) Close-up of one inclusion that exhibits a large area (in gray) corresponding to the deposition of the residue from the fluid in sample B16-1. The hole from which the fluid escaped

is visible at the center of the image, with the deposition forming a small channel and a large elongated area. **E)** Close-up of one open inclusion from which the fluid is lost in sample B16-1. Small remaining minerals, consisting of almost pure Ni and NiO, as shown by the EDX analyses in Table 2 (red crosses, inclusion 1), are still attached to the walls of the cavity. **F)** Close-up of one inclusion located in the same healed fracture in sample B16-1, which exhibits three different metallic alloys, as shown by the EDX analyses in Table 2 (red crosses, inclusion 2). The small holes represent the escape of a fluid phase, as indicated by the deposition at the surface on the left of the inclusion.

### 3.3 Micro-Raman analyses

#### 3.3.1. Primary inclusions

In-situ micro-Raman analyses of inclusions allowed for the identification of primary inclusions in samples B-6, B-16, B18-1 and B-20 (see Supplementary Materials, Table 1). The G and 2D (D overtone) modes of graphite (Ferrari, 2007) were identified in five selected diamonds (Figs. 8, 9 and displayed in Fig. 10). They are observed at variable wavenumbers of  $\sim 1583\text{-}1590\text{ cm}^{-1}$  and  $\sim 2726\text{-}2740\text{ cm}^{-1}$ , with the observed variability being possibly caused by a residual pressure effect. The high intensities of the Raman bands for diamond and graphite (Figs. 8B, D and F) made it difficult to observe other phases, if any were present. Modes in the hydroxyl stretching region ( $3200\text{-}3800\text{ cm}^{-1}$ ) are also present in all primary inclusions of samples B6-1, B18-1 and B20-1 (Figs. 8B, D, 10A and C), attesting to the presence of aqueous fluid-bearing inclusions.

Three Raman peaks observed at  $663$ ,  $990$  and  $1050\text{ cm}^{-1}$  in an isolated inclusion of sample B6-1 (Fig. 8A and 10A) are attributed here to breyite (formerly referred to as  $\text{CaSiO}_3$ -walsstromite; Brenker et al., 2020). In another inclusion from sample B6-1, breyite is associated with a different phase that has been identified as larnite,  $\beta\text{-Ca}_2\text{SiO}_4$  (Fig. 8C and 10B; Joswig et al., 1999). In sample B20-1, micro-Raman analysis revealed the presence of two inclusions of

breyite and larnite (Fig. 8E), and seven isolated primary inclusions of an unknown hydrous ferric sulfate phase. The Raman spectrum shows strong analogies with ferricopiapite,  $\text{Fe}^{3+}_2\text{Fe}^{3+}_4(\text{SO}_4)_6(\text{OH})_2 \cdot 20(\text{H}_2\text{O})$  (Figs. 8G, H and 10D), a mineral usually observed as a weathering or  $\text{Fe}^{3+}$  precipitation product. Further investigations would be required to characterize these hydrous ferric sulfate minerals.

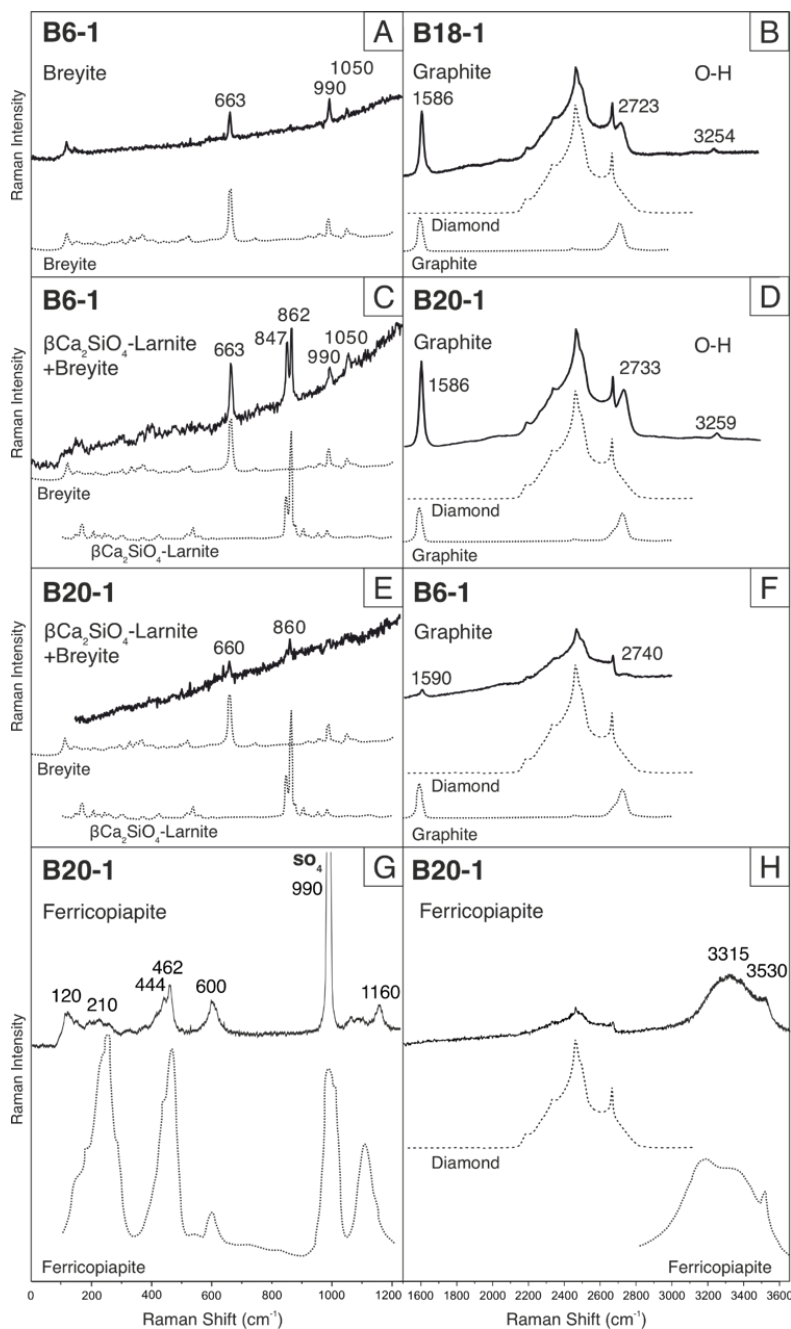


**Figure 8.** Raman spectroscopy analysis of primary inclusions. **A)** Primary isolated inclusion of breyite in sample B6-1. Reference spectra for breyite (dashed line) are from Anzolini et al. (2018). **B)** Graphite inclusion and water OH in sample B18-1, with graphite and diamond references from the RRUFF database. **C)** Primary inclusions of breyite and  $\text{Ca}_2\text{SiO}_4$ -larnite together in sample B6-1. **D)** Graphite inclusion, diamond and hydrous species (hydroxyl groups O-H) in sample B20-1. **E)** Potential presence of primary inclusions of breyite and  $\text{Ca}_2\text{SiO}_4$ -larnite in sample B20-1. The poor quality of the Raman spectra is attributed to the depth of the inclusions in the bulk diamond. **F)**

Graphite inclusion and diamond in sample B6-1. **G and H)** Unknown primary inclusion of a phase very close to a ferricopiapite, with reference taken from the RRUFF database.

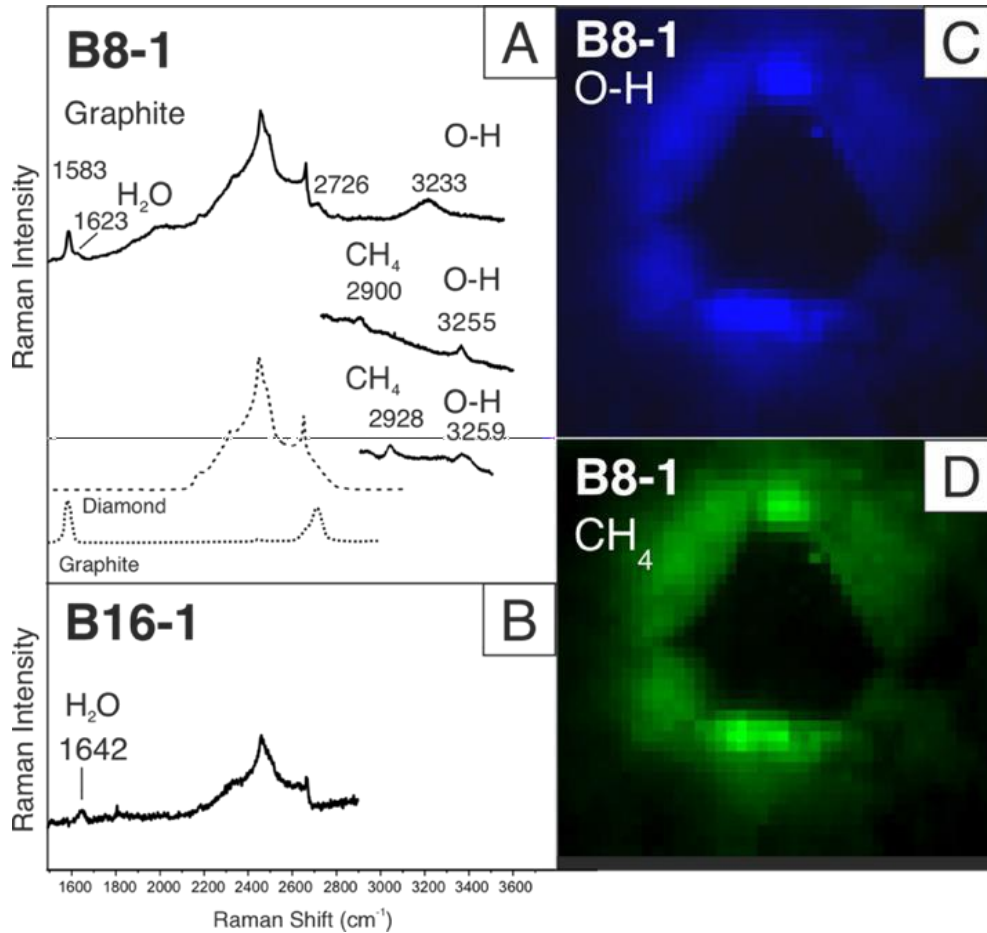


**Figure 9.** Raman spectroscopy analysis of secondary inclusions. **A)** Graphite and H<sub>2</sub>O (O-H stretching and HOH bending modes) measured in the central part of the secondary inclusion in sample B8-1 and **B)** in sample B16-1. The H<sub>2</sub>O signal indicates that the rim (i.e., the envelope surrounding the graphite crystals) is a fluid phase. **C)** Water O-H Raman mapping of a secondary inclusion in sample B8-1. **D)** Methane (CH<sub>4</sub>) Raman mapping of a secondary inclusion in sample B8-1. The high intensity of the graphite signal masks the fluid (OH, CH<sub>4</sub>) signal at the center of the maps.

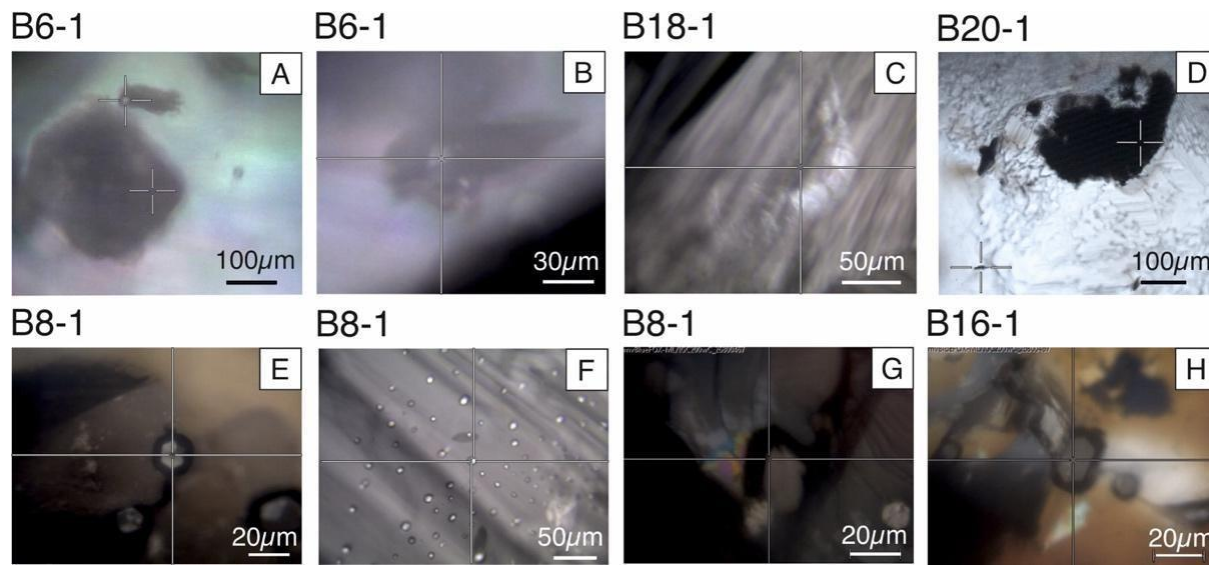


**Figure 10.** Images of some of the inclusions analyzed by Raman spectroscopy. The center of the cross indicates the location of analysis. **A)** Sample B6-1 inclusion of breyite. **B)** Sample B6-1 inclusion of breyite and  $\text{Ca}_2\text{SiO}_4$ -larnite. **C)** Sample B18-1 cluster of graphite containing a fluid phase. **D)** One inclusion of ferricopiapite located roughly fifteen micrometers below the surface of diamond B20-1. **E, F & G)** Secondary inclusions containing water and methane in sample B8-1 and **H)** in sample B16-1.

### 3.3.2. Secondary inclusions

Micro-Raman analyses were performed on the inclusions within the diamond with the main results displayed in Figs. 9 and 10. The multi-phased inclusions consist of central cubo-octahedral crystals identified as graphite (Ferrari, 2007), surrounded by an envelope consisting of small bands related to OH stretching mode from  $3255$  to  $3622\text{ cm}^{-1}$  (Figs. 9A and B), together with water at  $1642\text{ cm}^{-1}$  and methane ( $\text{CH}_4$ ) at  $\sim 2900\text{ cm}^{-1}$  (Figs. 9C and D). Although graphite + methane micro-inclusions were observed previously by Smit et al. (2016) in Marange (Zimbabwe) diamonds, to our knowledge, such multi-phased ( $\text{C}_{\text{graphite}}$ ,  $\text{H}_2\text{O}$ ,  $\text{CH}_4$ ) and cubo-octahedral-shaped inclusions have never before been reported in any type of natural diamond.



This assemblage recalls a high-pressure hydrous fluid, possibly parented to the diamonds, trapped as primary and secondary inclusions in the crystals.

### *3.4. SEM and EDX analyses*

#### *3.4.1. Secondary inclusions*

Successive cryo-milling perpendicularly crossing the healed fracture in sample B16-1 allowed for the exposure of secondary inclusions composed of different phases (Fig. 7C-F). These phases consist of crystals embedded in a fluid that was subsequently lost upon decrepitation, together with associated minerals (Figs. 7E and F). Fluid loss is inferred from the presence of a layer of residues deposited on the diamond surface (Figs. 7D and E) too thin to be quantitatively analyzed.

A few remaining solid phases are present within the rims of these fluid-bearing inclusions (Fig. 7E; inclusion 1), and depending on the position of the cryo-polishing, large minerals were exposed (Fig. 7F; inclusion 2). SEM-EDX analyses demonstrate that the inclusions contain several metallic alloys (Table 2; inclusions 1 and 2): a Ni-rich oxide containing Fe, Mg, Na, Si and Al (#1) and an almost pure Ni phase associated with Fe, Cr and Si (#2). Isolated inclusions of composite metallic alloys and sulfides also exhibit the same cubo-octahedral shape as graphite crystals characterized by Raman analyses (Figs. 7 E-F). A strong association between graphite layers and these metallic phases in other exposed secondary inclusions was observed. Additionally, a composite inclusion (Table 2: inclusion 2; Fig. 7F) exhibits a layer of a FeNi-rich phase associated with Cu alloy (#3) and a sulfide Fe-S phase with minor Cu (1.49 at%) (#4;

pyrrhotite group). The surface of inclusion 2 exposes small cavities most likely initially filled with a fluid (Fig. 7F).

**Table 2.** EDX analyses of two inclusions trapped in the healed fracture of sample B16-1 after the inclusions were exposed by ionic polishing. Analyses are summed to 100. Images of inclusions 1 and 2 are displayed in Figs. 7E and 7F, respectively. Inclusion 1 leaked during diamond opening and contains residual phases. Inclusion 2 contains a sulfide from the pyrrhotite group with Cu and is included in a layer of an alloy composed of Fe, Ni, Cu and a Ni-bearing ferricopiapite.

Element C (at%)	Fe	Ni	S	Cu	Cr	Si	O	Na	Mg	Al	Ca	K	Total
<b>Inclusion 1</b>													
#1	2.1	44.4				2.0	39.4	6.0	4.0	1.6	0.3	0.2	100
<b>Inclusion 2</b>													
#2	4.1	92.2			1.6	2.1							100
#3	55.6	42.0		2.4									100
#4	50.5		48.0	1.5									100
#5	42.1	15.0	16.0				26.9						100

### 3.5. X-ray fluorescence of primary and secondary inclusions

XRF in-situ micro-analyses of near-surface primary and secondary inclusions confirmed the presence of a metallic phase strongly associated with graphite (Fig. 11). Results further confirmed the presence of Fe-Ni-Cu alloys associated with graphite and the hydrous phase detected by micro-Raman spectroscopy and EDX. Metallic alloys are present in both secondary and primary inclusions in four diamonds (B6-1, B8-1, B16-1 and B20-1). Their nature – i.e., metallic alloys or oxides – cannot be determined by using these techniques alone.

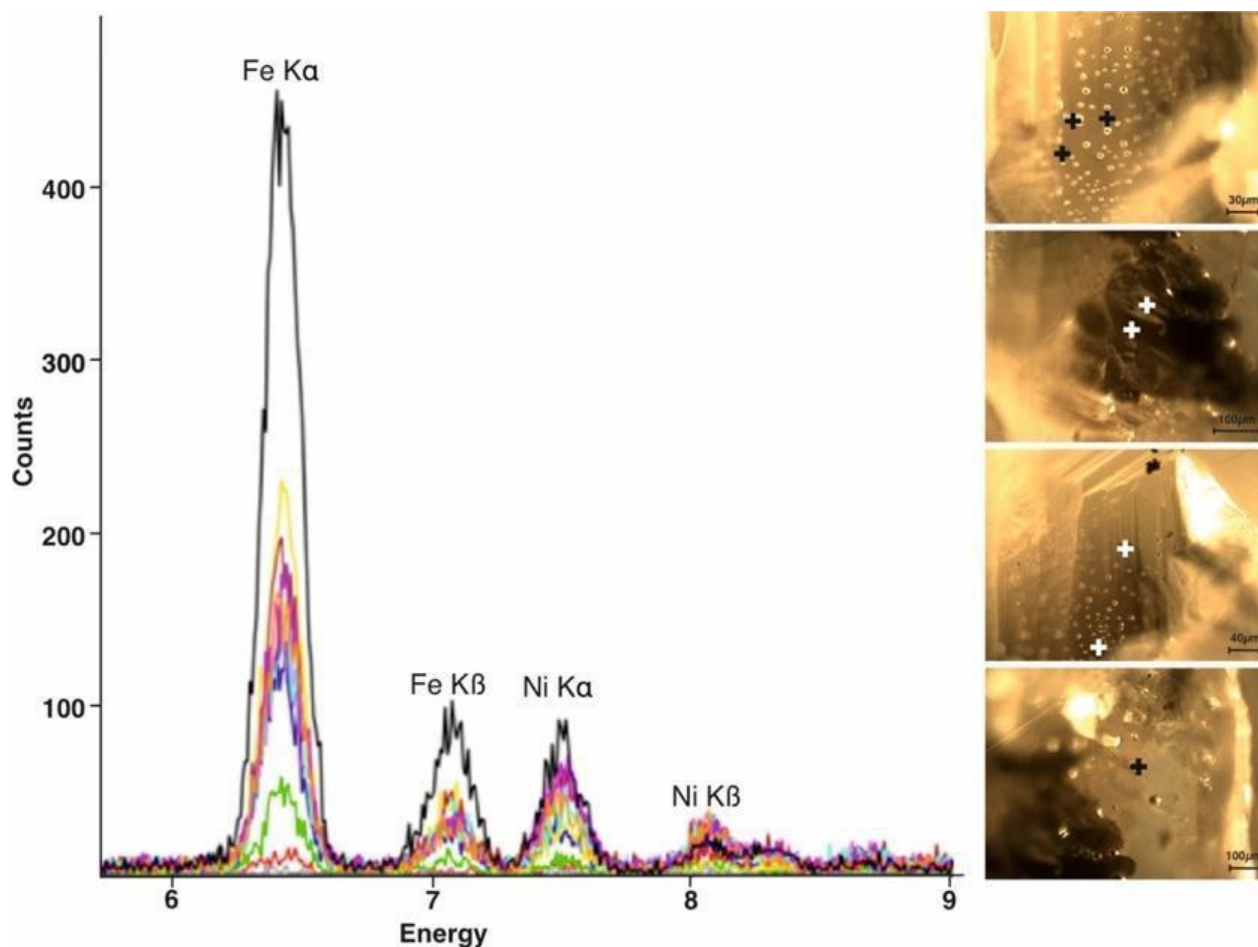


**Figure 11.** In-situ X-ray fluorescence measurements performed on inclusions of sample B8-1. Elements are identified thanks to the energy of their K- $\alpha$  and K- $\beta$  rays in KeV. Results indicate the presence of Fe-Ni-rich alloys in the cluster and in the isolated inclusions. It is not possible with this analysis to determine if they are native metals or oxides. For each spectrum, the area investigated is shown in the associated four images corresponding to different positions in the healed fracture. Crosses indicate locations in the large cluster and in the isolated inclusions where analyses were undertaken for the presence of metallic inclusions.

### 3.6. X-ray diffraction of primary and secondary inclusions

XRD analyses of both primary and secondary inclusions from three diamonds (B8-1, B16-1 and B20-1) revealed the presence of graphite in all inclusions and the coexistence of several phases, either trapped together or isolated (Table 3 and Supplementary Materials, Figs A-F).

**Table 3.** Diffraction patterns of selected inclusions in type IIb diamonds from SXRD micro-analysis. Synchrotron XRD patterns (wavelength 0.3738 Å) were processed with Rietveld refinement. *bcc*-(Fe,Ni) alloy indicates a mixture mainly composed of Fe, while *fcc*-(Ni,Fe) alloy is mainly composed of Ni.

#	Mineral phase	Unit cell parameters Å
B20-1-3	Graphite	a = 2.458, c = 6.443
	<i>bcc</i> -(Fe,Ni)	a = 2.861
	<i>fcc</i> -(Fe,Ni)	a = 3.572
B20-1-6	Graphite	a = 2.458, c = 6.419
	Breyite	a = 6.619, b = 9.213, c = 6.552, $\alpha = 83.4$ , $\beta = 75.99$ , $\gamma = 69.88$
	<i>fcc</i> -(Ni,Fe)	a = 3.570
B16-1-11	NiO	a = 4.187
B8-1-69	Graphite	a = 2.464, c = 6.716
	<i>bcc</i> -(Fe,Ni)	a = 2.868
	<i>fcc</i> -(Ni,Fe)	a = 3.588

No H<sub>2</sub>O ice (VI or VII) could be identified, which is consistent with the amorphous character of the hydrous phase either surrounding the graphite crystals in secondary inclusions (Figs. 5E and 5F) or forming the halo in primary inclusions (Fig. 5C).

In all investigated inclusions, Fe-Ni metallic phases are present, which is coherent with both the XRF investigation of samples B6-1, B8-1, B16-1 and B20-1 (Supplementary Materials Figs. A-F) and the EDX analyses of diamond B16-1 (Table 2). Furthermore, two different Fe-Ni

alloys have been identified using XRD: one Fe-rich alloy ( $\text{Ni} < 0.3$ ), which crystallized in the *bcc* group (hereafter referred to as “*bcc*-(Fe,Ni)”) and a Ni-rich alloy, which crystallized in the *fcc* group (referred to as “*fcc*-(Ni,Fe)”) (Table 3). If an ambient pressure is assumed, the *fcc*-(Ni,Fe) unit cell parameter would correspond to a composition of  $0.5 < \text{Ni} < 0.6$  (Cacciamani et al., 2010). However, it should be noted that since the unit-cell parameters are both pressure- and composition-dependent, it is not possible to determine the composition and remnant pressure from the XRD measurements alone. One inclusion exhibiting a rock-salt structure was identified in sample B16-1, with an XRD intensity peak consistent with NiO but likely with some substitutions with Fe or Mg, as indicated by both the unit-cell parameters and the SEM-EDX analyses. The XRD analyses of primary inclusions trapped in diamond B20-1 show that graphite and *fcc*-(Ni,Fe) are trapped together with a breyite inclusion. The cell parameters of the breyite indicate low residual pressures at ambient temperature.

### 3.7 Entrapment pressure calculation

The Raman spectrum of an isolated primary inclusion of breyite in diamond B6-1 exhibits three shifted peaks at 663, 990 and 1050  $\text{cm}^{-1}$  compared to the expected values of 656, 977 and 1037  $\text{cm}^{-1}$  at ambient conditions (Fig. 8A). Based on calibration curves obtained at different pressures by Anzolini et al. (2018), our observed Raman shifts on the B6-1 isolated breyite would correspond to a remnant pressure of 2.5 GPa (Anzolini et al., 2018). In diamond B20-1, graphite and hydrous phases coexist with primary inclusions which were identified by XRD as breyite, *fcc*-(Ni,Fe) and *bcc*-(Fe,Ni), while no oxides were detected. Assuming the experimental equation of state of Anzolini et al. (2016) and a unit cell volume of 363.78  $\text{\AA}^3$ , the residual pressure determined from the XRD patterns for B20-1 breyite is 2.8 GPa.

It has been shown that the potential presence of undetected micro-cracks in the host diamond surrounding breyite inclusions (even the smallest, with a diameter of  $< 12 \mu\text{m}$ ) may induce a pressure drop and an underestimation of the real diamond formation depth (Anzolini et al., 2016). To the best of our knowledge, breyite inclusions in B6-1 and B20-1 diamonds do not display decompression fractures of any sort. The similar residual pressures of 2.5 and 2.8 GPa calculated from isolated breyites contained in two different diamonds, and using two different techniques (micro-Raman spectroscopy and XRD), are evidence of the absence of decompression fractures, as their presence would otherwise result in random residual pressures. Based on the obtained remnant pressures from the Raman shifts and XRD measurements in the two isolated primary inclusions of breyite from samples B6-1 and B20-1, it is possible to calculate the minimal entrapment pressure of inclusions using elastic geothermobarometry (Angel et al., 2014). Trapping pressures were calculated using the EosFit-Pinc software (Angel et al., 2017). It is worth noting that both B6-1 and B20-1 diamonds contain other breyites, but, here, are associated with larnites (e.g., Fig. 10B). In presence of multi-phased inclusions, trapping pressures cannot be correctly calculated due to the risk of each of the mineral pairs reacting elastically in a different way, resulting in an underestimation of the remnant pressures (e.g., Cisneros and Befus, 2020). By applying a pressure correction induced by elastic relaxation, as proposed by Angel et al., (2017), a trapping pressure of 2.5 GPa at 900-1400 °C would result in a recalculated pressure of the isolated breyites in samples B6-1 and B20-1 ranging from 4.9 to 5.6 GPa, indicative of a formation depth between 160 to 180 km. Although these remain minimum estimated pressures, their consistency is striking, and collectively point to a lithospheric origin for the studied diamonds.

## 4. Discussion

### 4.1 *Where do type IIb diamonds form in the mantle?*

Consistent trapping pressure estimates from primary breyite inclusions in two different samples – as well as the mineralogy of their principal inclusions, such as larnite and graphite – suggest lithospheric formation depths between 160 to 180 km for our studied diamonds. Given that our proposed origin for type IIb diamonds could be distinct with some of the available literature, hereafter, we provide a review of breyite and larnite stability and genesis. Breyite and its high-pressure equivalent  $\text{CaSiO}_3$ -perovskite can be formed throughout the entire mantle and their presence alone in a diamond does not provide univocal evidence for a lower mantle origin (Moore and Helmstaedt 2019; Fedoraeva et al., 2019; Brenker et al. 2020). Indeed, breyite in diamonds have multiple origins. Some breyite can occur in lower mantle diamonds as a direct back-transformation product at 10 GPa of  $\text{CaSiO}_3$ -perovskite. However, Fedoraeva et al. (2019) have shown experimentally that breyite can also result from reaction between carbonate and  $\text{SiO}_2$  or a Si-rich fluid. The direct crystallization of both breyite and larnite (as observed in diamonds B6-1 and B20-1; Figs. 5A) can occur at pressures of 6 GPa slightly up to significantly higher and temperatures of 1300-1750 °C in a carbonate/Ca-rich environment (Fedoraeva et al., 2019). Temperatures required to reach the formation of breyite in Fedoraeva's experiments are slightly higher than those expected at the calculated lithospheric depths of our samples, but it is worth noting that our diamonds contain abundant aqueous fluids. We suggest that abundant available water would enable a sufficient decrease in temperatures during the reaction, allowing for the formation of breyite and larnite in the lithosphere, which would otherwise not be expected to occur at cratonic pressure-temperature conditions. In fact,

phase diagram interpretation indicates that the coexistence of breyite and larnite necessitates a trapping pressure within the range 6-9 GPa at 900-1400 °C at the lithosphere/asthenosphere boundary (Gasparik et al., 1994; Brenker et al., 2005 and 2007; Fedoraeva et al., 2019). Additionally, Fedoraeva et al. (2019) suggested that infiltration of a  $\text{CaCO}_3$ - $\text{CaSiCO}_3$  melt into a more reduced peridotitic mantle (see section 4.2) would result in a partial reduction of  $\text{CaCO}_3$  and precipitation of diamond, breyite and larnite at depths ranging from 160 to 180 km.

In conclusion, these are both viable scenarios for the formation of breyite and larnite inclusions at lithospheric depths in our studied diamonds. The association of Si-bearing inclusions and a water-rich fluid composition (large quantity of graphite-water inclusions) is coherent with the scenario of direct crystallization of both breyite and larnite at temperatures compatible with the cratonic lithosphere.

Demonstrating a sublithospheric origin of breyite or a  $\text{CaSiO}_3$  precursor would require its association with other inclusions such as ferropericlase, low-Ni enstatite (bridgmanite) or high pressure olivine polymorphs (e.g., Smith et al., 2018; Brenker et al., 2020). One such example is the association of ringwoodite with presumably secondary breyite observed in a sublithospheric type IIa diamond from Juina (sample JUC29; Pearson et al., 2014). None of these typical sublithospheric mineral phases were found in any of our diamonds. Furthermore, if the  $\text{H}_2\text{O}$  trapped in the type IIb diamonds studied here would have been trapped under sublithospheric conditions, it would be ice at room temperature (e.g. ice VII inclusions; Tschauer et al., 2018). The XRD investigation did not reveal any presence of any ice in the inclusions analyzed.

The lithospheric depths of diamond formation obtained from our recalculated residual pressures are also consistent with the presence of primary graphite inclusions (those not related



to the healed fractures; Fig. 10A-D), which points to the crystallization of diamonds close to the graphite-diamond inversion curve, corresponding to conditions of 4-4.5 GPa and 1200-1400 °C (e.g., Bulanova, 1995; Day, 2012). Based on the observed mineralogy in our samples and previous studies of Smith et al. (2018), we conclude that type IIb diamonds are capable, under certain conditions, of growing within a mantle continuum, ranging from lithospheric to sublithospheric depths.

#### *4.2 Type IIb diamond parental fluids*

This study documents that natural type IIb diamonds grow in the presence of fluids. This is a well-accepted concept, but the fluids can be diverse both chemically and from their redox state (oxidized or reduced). In this section, different models for diamond formation are reviewed in order to propose a credible scenario for lithospheric-grown type IIb diamonds.

Synthetic diamond growth typically occurs through carbon supersaturation of metallic alloys (e.g. Bataleva et al., 2016) and type IIb diamonds can be synthesized at lithospheric conditions, under reduced conditions. Chepurov et al. (2007) grew type IIb diamonds from a mixture of graphite as the carbon source, FeNi and FeCo alloys as solvents and B<sub>2</sub>O<sub>3</sub> as the boron source. Even if this mechanism contrasts with natural diamond formation complex redox reactions (e.g. Pal'Yanov et al., 2005, 2013), these synthetic diamonds show some similarities with our natural samples, in particular with respect to the occurrence of metallic inclusions.

The coexistence of reduced and oxidized species in diamonds suggests redox reactions: for example, Fe-C melt in equilibrium with FeO could dissolve up to 0.5 wt.% O (Sokol et al.,

2017). As it subsequently cools and crystallizes, oxygen would be released, yielding oxidized species.

Here, inclusions of primary Fe-Ni-Cu alloys, FeNi and FeNiO (Table 3), attest to the presence of metallic phases at lithospheric depths. This suggests that  $fO_2$  should be sufficiently low to stabilize Fe-alloys even at lithospheric pressures, where  $fO_2$  is generally considered to be above the iron-wüstite (IW) buffer (Shirey et al., 2013). This assemblage is rare but not unusual. Stachel et al. (1998) reported the presence of Fe, FeS, FeNiS and FeO inclusions and a solid solution of Fe-FeO-Fe<sub>3</sub>O<sub>4</sub> as inclusion in lithospheric diamonds from the Mwadui Mine, Tanzania. They also reported an inclusion consisting of a core of native iron rimmed by wüstite. Such an association might be interpreted as evidence of redox processes, possibly associated with oxidized fluids. Indeed, the presence of native iron, wüstite and magnetite in the same diamond might indicate a variation in oxygen fugacities from below iron-wüstite (IW) to above the wüstite-magnetite (WM) buffer. Stachel et al. (1998) proposed diamond formation over a large range of  $fO_2$  conditions, possibly along redox fronts. These conditions recall those of high-pressure (6 GPa) diamond synthesis from Mg-Ca-carbonates and metallic Fe at dry conditions (Pal'yanov et al., 2013). Diamonds would form both ahead of and behind the redox front because of the presence of a  $fO_2$  gradient. However, the above-cited studies do not consider the presence of water, as observed in the primary and secondary inclusions of the natural type IIb diamond studied here.

The presence of breyite and larnite in our diamonds could result from the reduction of Ca-rich silico-carbonatitic fluids enriched in solutes (Fedoraeva et al., 2019), consistent with the inclusions assemblage in diamond B16-1 (Table 2; Fig. 7E). Some experimental studies have

demonstrated the significant role played by carbonate-bearing hydrous fluids in the growth of diamonds (e.g., Pal'yanov et al., 1999; Sokol and Pal'yanov, 2008; Bureau et al., 2016; 2018) and as a vector for determining the diamond's carbon source (e.g. Weiss et al., 2014; Jablon and Navon, 2016 for natural samples).

In the type IIb diamonds analyzed in this study, diamond and graphite are in equilibrium together with abundant water. Both graphite and CH<sub>4</sub>-syngenetic inclusions were reported in mixed-habit Type Ia (i.e., N-bearing) diamonds from Marange in Zimbabwe (Smit et al., 2016). In the latter case, the intimate association of CH<sub>4</sub> and graphite suggests that both phases were trapped from the diamond parent fluid. In the diamond stability field, it has also been proposed that as hydrocarbon concentration in the aqueous fluid increases, initial diamond crystallization gives way to co-crystallization of both diamond and graphite, followed ultimately by crystallization of only graphite (Sokol et al., 2009).

In type IIb diamonds – and in Marange diamonds (Smit et al., 2016) – graphite would crystallize before diamond and would subsequently be trapped or serve as the seed for further diamond formation (Bulanova, 1995) during the fast diamond growth phase facilitated by the presence of water (Bureau et al., 2016). In this model, it is expected that diamonds should contain an abundance of nitrogen, as in the case of the Marange Mine diamonds. Here, however the absence of nitrogen could be explained by the presence of metal and sulfur that would prevent the nitrogen from being incorporated into the diamonds (see next section).

Stachel et al. (2017) suggested that diamond formation in peridotite would not occur with rock-buffered reactions, but rather would be buffered by the fluid itself, following the oxygen conservative reaction in the lithosphere (Deines, 1980):

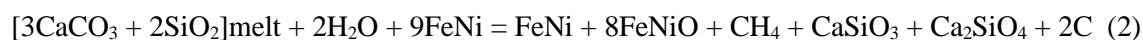


and assuming that all available  $\text{CO}_2$  (or carbonate solutes dissolved in a hydrous/silicic fluid or methane) is consumed during diamond and/or graphite crystallization. However, in this model, diamond growth is supposed to occur at the water maximum (i.e., for a fluid consisting almost exclusively of  $\text{H}_2\text{O}$  with minor  $\text{CH}_4$  and  $\text{CO}_2$ ; Foley, 2011; Stachel et al., 2017) and at near constant and buffered  $f\text{O}_2$  close to FMQ-1, -2 (Fayalite-Magnetite-Quartz), corresponding to the conditions of the redox EMOD reaction (Stachel et al., 2017). This model contrasts with the presence of metallic liquids mingled with the aqueous fluid observed in type IIb diamonds. Type IIb diamond formation may be closer to the model for crystallization of Fe alloys, in association with diamonds that reacted with a surrounding silicate proposed by Jacob et al. (2004). Citing a polycrystalline diamond of inferred lithospheric provenance exhibiting cohenite, native iron and troilite enclosed within a garnet inclusion, they suggest that the inclusions in the garnets reflect local and probably transient conditions within the lithosphere, linked to diamond formation within a C-O-H fluid that reacted with the surrounding silicate.

One could argue that the source of carbon for diamond growth may be a metallic liquid (e.g., Smith et al., 2016), as experimentally achieved from mixture of FeNiS metals and iron carbides at mantle conditions (Bataleva et al., 2016). In the absence of iron carbides, carbon may be dissolved in these metallic melts, as demonstrated, for example, by experimental pressures of 1-15 GPa and temperatures of 1600-2300 °C inducing the solubility of carbon in FeNi metallic liquids in equilibrium with silicates reaching a few wt.% (e.g., Malavergne et al., 2019). Carbide melt is a possible source medium proposed by Smith and co-authors (2014; 2016). However, carbide inclusions (i.e. cohenite) were not found in our studied type IIb diamonds. Our data

illustrate that the mantle environment where these type IIb diamonds grew is particularly rich in water. In a FeNiC melt, with even the slightest presence of water in the melt (>0.5 % of water), diamond growth would be inhibited, with graphite forming instead of diamond (Pal'yanov et al., 2012).

Rather, type IIb diamond formation may be described by the following simplified equation:



In this scenario, multiple carbon source are possible:  $\text{CO}_3^{2-}$  or  $\text{CO}_2$  dissolved in a melt and possibly trace amount of C initially dissolved and released during crystallization of FeNi and FeNiO.

Based on the presence of Ca-bearing silicate minerals and C-O-H fluids in the studied diamonds, the above scenario, involving carbonate reduction would release methane, metal alloys and metal oxides, and silicate minerals, such as breyite and larnite, trapped in type IIb diamonds during their syngenetic growth. In this model, N would be sequestered/scavenged by the metallic phase (Sokol et al., 2019) and/or by sulfur. Type IIb diamonds growing in fluids introduced in highly reduced conditions would thus not incorporate any nitrogen. In this model the graphite- $\text{CH}_4$  assemblage would represent the residual rather than the primitive fluid.

#### *4.3. B- and N- poor type IIb diamonds: the key to identifying their growth environment*

Nitrogen content in diamonds, including its core-to-rim variations, is commonly interpreted as relating to their host fluid through their melt/fluid-diamond partitioning coefficient

(Deines et al., 1989; Cartigny et al., 2001; Stachel et al., 2009), with this interpretation having been used in previous studies (e.g. Thomassot et al., 2007; Smit et al., 2016).

The occurrence of boron in type IIb diamonds has led to the widespread adoption of the term “boron-rich diamond”. Linking type IIb diamond genesis with fluids derived from “B-rich environments”, in particular subducted serpentinites (e.g., Smith et al., 2018a), however, suffers from several shortcomings. Notably, B-recycling in the mantle, at depths beyond those of the back-arc (100 km), is the object of ongoing debate (De Hoog and Savov, 2018), with some researchers suggesting recently that boron is actually not subducted in the deep mantle at all (McCaig et al., 2018). Furthermore, with a maximum B value of 10 atomic ppm, the B/C-ratios of type IIb diamonds are low,  $< 10 \times 10^{-6}$ , with this value remaining approximately three orders of magnitude lower than that of the depleted or primitive mantle (B/C-ratio of approximately  $6800 \times 10^{-6}$ , computed from  $\sim 0.3$  ppm B and  $\sim 49$  ppm C; McDonough and Sun, 1995; Chaussidon and Jambon, 1994; Cartigny et al., 2008; Le Voyer et al., 2017). Thus, the need to relate type IIb diamonds to B-rich subducted serpentinites appears unjustified given that Earth’s mantle is sufficiently rich in boron at  $\sim 8$  ppm to account for the B-content of type IIb diamonds (Gaillou et al., 2012).

In our view, the fundamental observation informing the origin of type IIb diamonds is not related to the occurrence of “high” boron content in these diamonds, but rather their low B-content coupled with even lower levels of nitrogen. Both the convective mantle and subducted serpentinite derived fluids/melts contain substantial amounts of nitrogen (e.g. Cartigny and Marty, 2013 for a review of mantle nitrogen; Philippot et al., 2007; Cannàò et al., 2020 for a

review of subducted serpentinites. Even with available boron present, nitrogen would prevent it from expressing the typical spectroscopic features found in type IIb diamonds.

Nitrogen partitioning ( $K_d$ -values) between fluid and diamond has been deduced or suggested in a number of previous studies, though the extent to which the phenomenon is said to occur varies substantially and no consensus has yet been reached (e.g., Cartigny et al., 2014 for a review on the subject). In the case of  $\text{CH}_4$ -rich fluids, two phenomena would be expected to occur: given the compatible behavior of N (Thomassot et al., 2007; Stachel et al., 2017), the fluid would become increasingly N-depleted with the progression of diamond crystallization while simultaneously becoming  $^{13}\text{C}$ -depleted owing to the partitioning of C-isotopes between diamond and  $\text{CH}_4$  (Cartigny et al., 2014). These diamonds would therefore have both low  $\delta^{13}\text{C}$ -values, as can be inferred from the few available data for large type II diamonds (from -20.8 to -1.8‰ vs. V-PDB; Milledge et al., 1983; Smith et al., 2018a), as well as to having low N-contents, making the presence of boron in these diamonds possible only when the partitioning value of boron in the fluid is less than that of nitrogen. To the best of our knowledge, no  $K_d$ -values between fluid and diamond have been determined for boron, leaving open the possibility that type IIb diamonds indeed grow from fluids with high B/C-ratios, albeit with very low  $K_d$ -values (i.e., boron would be incompatible with respect to diamond). Given that significant amounts of boron (> 1000 at.ppm) can be incorporated into synthetic diamonds (Polyakov et al., 2001), the low B-content of type IIb diamonds might reflect low B/C-ratios of the parental fluid at elevated  $K_d$ -values (i.e., > 1). Still, a preferable explanation is that the low N-character reflects low oxygen fugacity. Under metal-saturation conditions, nitrogen would be sequestered in the metal phase (Sokol et al., 2019), whether the fluid derives from a reduced environment or, as documented

here, from crystallization of the diamond in oxidized fluids introduced into a reduced environment. Bolstering this argument, experimental studies have suggested that in the metal-fluid system, nitrogen has a higher affinity for iron and selectively accumulates in the metal phase, while some mobile carbon resides in the fluid phase (Sokol et al., 2018).

The sequestration of N in metals can explain the absence of nitrogen in large sublithospheric type II diamonds carrying metallic inclusions (Smith and Kopylova, 2014; Smith et al, 2016). Given that boron is a lithophile element, the fluids/melts would, in a reduced environment, develop rather high B/N-ratios. In this case, B-poor, nitrogen-free type IIb diamonds would characterize the most reduced environment for diamond formation. An alternative hypothesis for explaining the absence of N could be related to its speciation in the mantle as  $N_2$  or  $NH_4^+$ , both of which are incompatible in the diamond lattice into which nitrogen substitutes for carbon as single atoms (Mikhail and Howell, 2016).

## **5. Conclusions**

A detailed study of type IIb diamonds from the Cullinan Mine, South Africa, allowed identification of hydrous fluids in primary and secondary inclusions, associated with methane, graphite, metallic alloys, sulfides and oxides. The most important conclusions of this study are:

- 1) The mineralogical assemblage of primary inclusions shows the presence of breyite  $\pm$  larnite and graphite. Breyite inclusions were used to estimate residual pressures of 2.5-2.8 GPa corresponding to minimum entrapment pressures of 4.9 to 5.6 GPa at the typical temperature range of 900-1400°C, otherwise known as the “diamond window”. These physical conditions – together with the presence of breyite  $\pm$  larnite and graphite



inclusions and the absence of typical sublithospheric mineral association of  $\text{CaSiO}_3$  + ferropericlase, low-Ni enstatite or olivine polymorphs – are more consistent with lithospheric depths of formation for type IIb diamonds, which were, until now, considered only of sublithospheric origin (Smith et al., 2018a and b).

- 2) The type IIb diamonds studied here revealed numerous mineral and fluid inclusions: a hydrous phase ( $\text{H}_2\text{O}$ , OH) with  $\text{CH}_4$  and solute, Fe-Ni oxides, hydrous ferrous sulfates and Fe-Ni±Cu alloys. The coexistence of reduced and oxidized species suggests redox reactions, where the  $f\text{O}_2$  should be sufficiently low for Fe-alloys to be stable under lithospheric pressures; it may reflect local and probably transient conditions within the lithosphere (Jacob et al., 2004), linked to the equilibrium of diamond with C-O-H fluids such as those identified in the studied type IIb diamonds.
- 3) Finally, the lack of nitrogen and the presence of only negligible boron in type IIb diamonds does not ultimately require a link with the subduction setting, given Earth's mantle is sufficiently B-rich to account for the formation of type IIb diamonds, while simultaneously nitrogen is likely sufficiently sequestered by metallic alloys accompanying growth fluids to explain its absence.

It is not the intent of the authors here to refute the sublithospheric origin of type IIb blue diamonds proposed by Smith et al. (2018a, b) and based on mineral assemblages typical of the lower mantle. Rather, we contend, based on our results suggesting lithospheric depths of formation, that type IIb diamonds form in a mantle continuum, from sublithospheric to lithospheric depths. In proposing this new framework for type IIb diamond formation and discussing the conditions under which it is viable, this work highlights the limited knowledge

available concerning these peculiar diamonds, stemming principally from the paucity of samples to study. The mineral and fluid inclusion assemblages observed here, together with previous results from Smith et al. (2018a,b), will be crucial in developing a well-constrained model of the formation of type IIb diamonds. Meanwhile, boron isotope measurement on type IIb diamonds, yet difficult to determine with precision, will be a major step to decipher the source of boron in blue diamonds.

### **Acknowledgements**

This manuscript benefited from informal reviews from Ingrid Chinn and Thomas Stachel of earlier versions of the manuscript. The handling editor S. Aulbach, Alex Sokol and an anonymous reviewer are thanked for their constructive and thoughtful criticisms. We greatly acknowledge De Beers Consolidated Mines for the donation of the diamonds, including Ingrid Chinn for her support. This project is funded by Sorbonne Université EMERGENCE program (HYDRODIAMS to HB), TelluS Program of the CNRS-INSU, GEOTOP and FRQNT for an international internship to LD, and NSERC Discovery grant RGPIN-2015-05378 for funding LD doctoral fellowship. The SEM facility of IMPMC is supported by Région Ile de France Grant SESAME 2006 NOI-07-593/R, INSU-CNRS, INP-CNRS, UPMC, and by the French National Research Agency (ANR) Grant ANR-07-BLAN-0124-01. The authors wish to acknowledge the French Gem Lab LFG (Laboratoire Français de Gemmologie) for confirming some of the FTIR results, especially Annabelle Herreweghe and Stefanos Karampelas. We thank M. Guillaumet from the IMPMC spectroscopy platform, Ludovic Delbes, Philippe Rosier from the IMPMC cellule project, and Christophe Sandt and Ferenc Borondics from the SMIS beamline at SOLEIL

synchrotron for their support during micro-Raman spectral imaging. We thank Ross Angel for his kind help and advice on the calculation of pressure correction for elastic relaxation.

## References

- Allsopp, H.L., Bristow, J.W., Smith, C.B., Brown, R., Gleadow, A.J.W., Kramers, J.D., Garvie, O.G., 1989. A summary of radiometric dating methods applicable to kimberlites and related rocks. Geological Society Australia Special Publication 14, 343–357.
- Angel, R.J., Mazzucchelli, M.L., Alvaro, M., Nimis, P., Nestola, F., 2014. Geobarometry from host-inclusion systems: the role of elastic relaxation. *American Mineralogist* 99, 2146-2149.
- Angel, R.J., Mazzucchelli, M.L., Alvaro, M., Nestola, F., 2017 EosFit-Pic: a simple GUI for host-inclusion elastic thermobarometry. *American Mineralogist* 102, 1957-1960.
- Anthony, J.W., Bideaux, R.A., Bladh, K.W. and Nichols, M.C., 2000. Handbook of Mineralogy, Volume 4, Arsenates, Phosphates, Vanadates: Tucson, Arizona, Mineral Data Publishing.
- Anzolini, C., Angel, R.J., Merlini, M., Derzsi, M., Tokár, K., Milani, S., Harris, J.W., 2016. Depth of formation of CaSiO<sub>3</sub>-walstromite included in super-deep diamonds. *Lithos* 265, 138-147.
- Anzolini, C., Prencipe, M., Alvaro, M., Romano, C., Vona, A., Lorenzon, S., Nestola, F., 2018. Depth of formation of super-deep diamonds: Raman barometry of CaSiO<sub>3</sub>-walstromite inclusions. *American Mineralogist* 103, 69-74.

- Auer, B.M., Skinner, J.L., 2008. IR and Raman spectra of liquid water: Theory and interpretation. *Journal of Chemical Physics* 128, 224511.
- Bataleva, Y.V., Palyanov, Y.N., Borzdov, Y.M., Sobolev, N.V. 2016. Graphite and diamond formation via the interaction of iron carbide and Fe,Ni-sulfide under mantle P–T parameters. *Doklady Earth Sciences* 471,1144-1148.
- Brenker, F.E., Vincze, L., Vekemans, B., Nasdala, L., Stachel, T., Vollmer, C., Kersten, M., Somogyi, A., Adams, F., Joswig, W., Harris, J.W., 2005. Detection of Ca-rich lithology in the Earth's deep (> 300) convecting mantle. *Earth and Planetary Science Letters* 236, 579-587.
- Brenker, F.E., Nestola, F., Brenker, L., Peruzzo, L., Harris, J.W., 2020. Origin, properties and structure of breyite: the second most abundant mineral inclusion in super-deep diamonds. *American Mineralogist* 106, 38-43.
- Bulanova, G.P., 1995. The formation of diamond. *Journal of Geochemical Exploration* 53, 1-23.
- Bureau, H., Frost, D.J., Bolfan-Casanova, N., Leroy, C., Esteve, I., Cordier, P., 2016. Diamond growth in mantle fluids, *Lithos* 265, 4-15.
- Bureau, H., Remusat, L., Esteve, I., Pinti, D.L., Cartigny, P., 2018. The growth of lithospheric diamonds. *Science Advanced* 4, 1602-1607.
- Cacciamani, G., Dinsdale, A., Palumbo, M., Pasturel, A., 2010. The Fe–Ni system: thermodynamic modelling assisted by atomistic calculations. *Intermetallics* 18, 1148-1162.

- Cannaò, E., Tiepolo, M., Bebout, G.E., Scambelluri, M., 2020. Into the deep and beyond: Carbon and nitrogen subduction recycling in secondary peridotites. *Earth and Planetary Science Letters* 543, 116328.
- Cartigny, P., Harris, J.W., Javoy, M. 2001. Diamond genesis, mantle fractionations and mantle nitrogen content: a study of  $\delta^{13}\text{C-N}$  concentrations in diamonds. *Earth and Planetary Sciences Letters* 185, 85-98.
- Cartigny, P., Pineau, F., Aubaud, C., Javoy, M., 2008. Towards a consistent mantle carbon flux estimate: Insights from volatile systematics ( $\text{H}_2\text{O/Ce}$ ,  $\delta\text{D}$ ,  $\text{CO}_2/\text{Nb}$ ) in the North Atlantic mantle ( $14^\circ\text{N}$  and  $34^\circ\text{N}$ ). *Earth and Planetary Science Letters* 265, 672-685.
- Cartigny, P., Marty, B., 2013. Nitrogen isotopes and mantle geodynamics: The emergence of life and the atmosphere–crust–mantle connection. *Elements* 9, 359-366.
- Cartigny, P., Palot, M., Thomassot, E., Harris, J.W., 2014. Diamond formation: a stable isotope perspective. *Annual Review of Earth and Planetary Sciences* 42, 699-732.
- Chaussidon, M., Jambon, A., 1994. Boron content and isotopic composition of oceanic basalts: geochemical and cosmochemical implications. *Earth and Planetary Science Letters* 121, 277-291.
- Chepurov, A.I., Zhimulev, E.I., Fedorov, I.I., Sonin, V.M., 2007. Inclusions of metal solvent and color of boron-bearing monocrystals of synthetic diamond. *Geology of Ore Deposits* 49, 648-651.
- Chrenko, R.M., 1973. Boron, the dominant acceptor in semiconducting diamond. *Physical Review B* 7, 4560-4567.

- Cisneros, M., Befus, K. S. (2020). Applications and limitations of elastic thermobarometry: Insights from elastic modeling of inclusion-host pairs and example case studies. *Geochemistry, Geophysics, Geosystems*, 21, e2020GC009231.
- Collins A.T., 1982. Colour centres in diamond. *Journal of Gemmology*, Vol. 18, No. 1, pp. 37-75.
- Day, H. W., 2012. A revised diamond-graphite transition curve. *American Mineralogist*, 97(1), 52-62.
- De Hoog, J.C.M., Savov, I.P., 2018. Boron isotopes as a tracer of subduction zone processes, in: Marschall, H., Foster, G. (Eds.), *Boron Isotopes: The Fifth Element*, pp. 217-247.
- Deines, P., 1980. The carbon isotopic composition of diamonds: relationship to diamond shape, color, occurrence and vapor composition. *Geochimica et Cosmochimica Acta* 44, 943-961.
- Deines, P., Harris, J.W., Spear, P.M., Gurney, J.J., 1989. Nitrogen and <sup>13</sup>C content of Finsch and Premier diamonds and their implications. *Geochimica et Cosmochimica Acta* 53, 1367-1378.
- Downs, R.T., Hall-Wallace, M., 2003. The American Mineralogist crystal structure database. *American Mineralogist* 88, 247-250.
- Fedoraeva, A.S., Shatskiy, A., Litasov, K.D., 2019. The join CaCO<sub>3</sub>-CaSiO<sub>3</sub> at 6 GPa with implication to Ca-rich lithologies trapped by kimberliteic diamonds. *High Pressure Research*, 39, 547-560.

- Ferrari, A.C., 2007. Raman spectroscopy of graphene and graphite: Disorder, electron–phonon coupling, doping and nonadiabatic effects. *Solid State Communications* 143, 47-57.
- Fisher, D., Sibley, S.J., Kelly, C.J., 2009. Brown colour in natural diamond and interaction between the brown related and other colour-inducing defects. *Journal of Physics: Condensed Matter*, 21, 1-10.
- Frost, D.J., McCammon, C.A., 2008. The redox state of Earth's mantle. *Annual Review of Earth and Planetary Sciences* 36, 389-420.
- Foley, S. F., 2011. A Reappraisal of Redox Melting in the Earth's Mantle as a Function of Tectonic Setting and Time, *Journal of Petrology*, Volume 52, Issue 7-8, Pages 1363–1391.
- Gaillou, E., Post, J.E., Rost, D., Butler, J.E., 2012. Boron in natural type IIb blue diamonds: Chemical and spectroscopic measurements. *American Mineralogist* 97, 1-18.
- Gasparik, T., Wolf, K., Smith, C.M., 1994. Experimental determination of phase relations in the  $\text{CaSiO}_3$  system from 8 to 13 GPa. *American Mineralogist* 79, 1219-1222.
- Glinnemann, J., Kusaka, K., Harris, J.W., 2003. Oriented graphite single-crystal inclusions in diamond. *Zeitschrift für Kristallographie-Crystalline Materials* 218, 733-739.
- Harte, B., 2010. Diamond formation in the deep mantle: the record of mineral inclusions and their distribution in relation to mantle dehydration zones. *Mineralogical Magazine* 74, 189–215.
- Jablon, B.M., Navon, O. 2016. Most diamonds were created equal. *Earth and Planetary Sciences Letters* 443, 41-47.

- Jacob, D.E., Kronz, A., Viljoen, K.S., 2004. Coehnite, native iron and troilite inclusions in garnets from polycrystalline diamond aggregates. *Contribution to Mineralogy and Petrology*, 146, 566-576.
- Joswig, W., Stachel, T., Harris, J. W., Baur, W. H., Brey, G. P., 1999. New Ca-silicate inclusions in diamonds—tracers from the lower mantle. *Earth and Planetary Science Letters*, 173(1-2), 1-6.
- King, J.M., Moses, T.M., Shigley, J.E., Welbourn, C.M., Lawson, S.C., Cooper, M., 1998. Characterizing natural-color type IIb blue diamonds. *Gems & Gemology* 34, 246-268.
- Le Voyer, M., Kelley, K.A., Cottrell, E., Hauri, E.H., 2017. Heterogeneity in mantle carbon content from CO<sub>2</sub>-undersaturated basalts. *Nature Communications* 8, 14062.
- Malavergne, V., Bureau, H., Raepsaet, C., Gaillard, F., Poncet, M., Surblé, S., Sifré, D., Shcheka, S., Fourdrin, C., Deldicque, D., Khodja, H., 2019. Experimental constraints on the fate of H and C during planetary core-mantle differentiation. Implications for the Earth. *Icarus* 321, 473-485.
- McCaig, A.M., Titarenko, S.S., Savov, I.P., Cliff, R.A., Banks, D., Boyce, A., Agostini, S., 2018. No significant boron in the hydrated mantle of most subducting slabs. *Nature Communications* 9, 4602.
- McDonough, W.F., Sun, S.-S., 1995. The composition of the Earth. *Chemical Geology* 120, 223-253.
- Men, Z., Fang, W., Li, D., Li, Z., Sun, C., 2014. Raman spectra from symmetric hydrogen bonds in water by high-intensity laser-induced breakdown. *Scientific Reports* 4, 4606.



- Meyer H O A 1987 Mantle Xenoliths ed P H Nixon (Chichester: Wiley) pp 501–22
- Mikhail, S., Howell, D., 2016. A petrological assessment of diamond as a recorder of the mantle nitrogen cycle. *American Mineralogist*, 101, 780-787.
- Milledge, H.J., Mendelsohn, M.J., Seal, M., Rouse, J.E., Swart, P.K., Pillinger, C.T., 1983. Carbon isotopic variation in spectral type II diamonds. *Nature* 303, 791-792.
- Moore, A. E., Helmstaedt, H., 2019. Evidence for two blue (type IIb) diamond populations. *Nature* 570, E26-E27.
- Moser, D.E., Flowers, R.M., Hart, R.J., 2001. Birth of the Kaapvaal tectosphere 3.08 billion years ago. *Science* 291, 465-469.
- Nestola, F., Korolev, N., Kopylova, M., Rotiroti, N., Pearson, D.G., Pamato, M.G., Alvaro, M., Peruzzo, L., Gurney, J.J., Moore, A.E., Davidson, J., 2018. CaSiO<sub>3</sub> perovskite in diamond indicates the recycling of oceanic crust into the lower mantle. *Nature* 555, 237-241.
- Pal'yanov Y.N., Sokol A.G., Bozdov Y.M., Khokhryakov A.F., Sobolev N.V., 1999. Diamond formation from mantle carbonate fluids. *Nature* 400, 417–418.
- Pal'yanov, Y.N., Sokol, A.G., Tomilenko, A.A., Sobolev, N.V., 2005. Conditions of diamond formation through carbonate-silicate interaction. *European Journal of Mineralogy* 17, 207–214
- Palyanov, Y. N., Borzdov, Y. M., Kupriyanov, I. N., Khokhryakov, A. F., 2012. Effect of H<sub>2</sub>O on diamond crystal growth in metal–carbon systems. *Crystal growth & design*, 12(11), 5571-5578.

- Pal'yanov, Y.N., Bataleva, Y.V., Sokol, A.G., Borzdov, Y.M., Kupriyanov, I.N., Reutsky, V.N., Sobolev, N.V., 2013. Mantle–slab interaction and redox mechanism of diamond formation. *Proceedings of the National Academy of Sciences* 110, 20408-20413.
- Pearson, D. G., Brenker, F. E., Nestola, F., McNeill, J., Nasdala, L., Hutchison, M. T., Matveev, S., Mather, K., Silversmit, G., Schmitz, S., Vekemans, B., Vincze, L., 2014. Hydrous mantle transition zone indicated by ringwoodite included within diamond. *Nature*, 507(7491), 221-224.
- Philippot, P., Busigny, V., Scambelluri, M., Cartigny, P., 2007. Oxygen and nitrogen isotopes as tracers of fluid activities in serpentinites and metasediments during subduction. *Mineralogy and Petrology* 91, 11-24.
- Polyakov, V.I., Rukovishnikov, A.I., Rossukanyi, N.M., Ralchenko, V.G., 2001. Electrical properties of thick boron and nitrogen contained CVD diamond films. *Diamond and Related Materials* 10, 593-600.
- Prescher, C., Prakapenka, V.B., 2015. DIOPTAS: a program for reduction of two-dimensional X-ray diffraction data and data exploration. *High Pressure Research* 35, 223–230.
- Reich, S., Thomsen, C., 2004. Raman spectroscopy of graphite. *Philosophical Transactions of the Royal Society of London. Series A: Mathematical, Physical and Engineering Sciences* 362, 2271-2288.
- Roedder, E., 1979. Origin and significance of magmatic inclusions. *Bull. Mineral.* 102, 487-510.

- Schmitz, M.D., Bowring, S.A., de Wit, M.J., Gartz, V., 2004. Subduction and terrane collision stabilize the western Kaapvaal craton tectosphere 2.9 billion years ago. *Earth and Planetary Science Letters* 222, 363-376.
- Schrauder, M., Navon, O., 1994. Hydrous and carbonatitic mantle fluids in fibrous diamonds from Jwaneng, Botswana. *Geochimica et Cosmochimica Acta*, 58(2), 761-771.
- Scoates, J.S., Friedman, R.M., 2008. Precise age of the platiniferous Merensky Reef, Bushveld Complex, South Africa, by the U–Pb zircon chemical abrasion ID-TIMS technique. *Economic Geology* 103, 465–471.
- Shatsky, V. S., Ragozin, A. L., Logvinova, A. M., Wirth, R., Kalinina, V. V., Sobolev, N. V., 2020. Diamond-rich placer deposits from iron-saturated mantle beneath the northeastern margin of the Siberian Craton. *Lithos*, 364, 105514.
- Shirey, S. B., Cartigny, P., Frost, D. J., Keshav, S., Nestola, F., Nimis, P., Pearson, G., Sobolev, N. V., Walter, M. J., 2013. Diamonds and the geology of mantle carbon. *Reviews in Mineralogy and Geochemistry*, 75(1), 355-421.
- Shirey, S.B., Smit, K., Pearson, G., Walter, M. J., Aulbach, S., Brenker, F. E., Bureau, H., Burnham, A. D., Cartigny, P., Chacko, T., Frost, D. J., Hauri, E. J., Jacob, D. E., Jacobsen, S. D., Kohn, S. C., Luth, R. W., Mikhail, S., Navon, O., Nestola, F., Nimis, P., Palot, M., Smith, E. M., Stachel, T., Stagno, V., Steele, A., Stern, R. A., Thomassot, E., Thomson, A. R., Weiss, Y., , 2019. Diamonds and the mantle geodynamics of carbon: deep mantle carbon evolution from the diamond record, in: Orcutt, B., Daniel, I. Dasgupta, R. (Eds.), *Deep Carbon: Past to Present* . Cambridge University Press, Cambridge, pp. 89-128.

- Smit, K.V., Shirey, S.B., Stern, R.A., Steele, A., Wang, W., 2016. Diamond growth from C–H–N–O recycled fluids in the lithosphere: Evidence from CH<sub>4</sub> micro-inclusions and  $\delta^{13}\text{C}$ – $\delta^{15}\text{N}$ –N content in Marange mixed-habit diamonds. *Lithos* 265, 68-81.
- Smith, E.M., Kopylova, M., 2014. Implications of metallic iron for diamonds and nitrogen in the sublithospheric mantle. *Canadian Journal of Earth Sciences* 51, 510-516.
- Smith, E.M., Shirey, S.B., Nestola, F., Bullock, E.S., Wang, J., Richardson, S.H., Wang, W., 2016. Large gem diamonds from metallic liquid in Earth's deep mantle. *Science* 354, 1403-1405.
- Smith, E.M., Shirey, S.B., Richardson, S.H., Nestola, F., Bullock, E.S., Wang, J., Wang, W., 2018a. Blue boron-bearing diamonds from Earth's lower mantle. *Nature*, 560, 84-87.
- Smith, E.M., Shirey, S.B., Richardson, S.H., Nestola, F., Bullock, E.S., Wang, J., Wang, W., 2018b. Reply to: Evidence for two blue (type IIb) diamond populations. *Nature* 570, doi.org/10.1038/s41586-019-1246-8.
- Smith, E. M., Ni, P., Shirey, S. B., Richardson, S. H., Wang, W., Shahar, A., 2021. Heavy iron in large gem diamonds traces deep subduction of serpentinized ocean floor. *Science Advances*, 7(14), eabe9773.
- Sokol, A.G., Pal'yakov, Y.N., 2008. Diamond formation in the system MgO–SiO<sub>2</sub>–H<sub>2</sub>O–C at 7.5 GPa and 1600 °C. *Contribution to Mineralogy and Petrology* 155, 33–43.
- Sokol, A. G., Palyanova, G. A., Palyanov, Y. N., Tomilenko, A. A., & Melenevsky, V. N., 2009. Fluid regime and diamond formation in the reduced mantle: Experimental constraints. *Geochimica et Cosmochimica Acta*, 73(19), 5820-5834.

- Sokol, A. G., Kruk, A. N., Seryotkin, Y. V., Korablin, A. A., & Palyanov, Y. N., 2017. Phase relations in the Fe-Fe<sub>3</sub>C-Fe<sub>3</sub>N system at 7.8 GPa and 1350° C: Implications for carbon and nitrogen hosts in FeO-saturated upper mantle. *Physics of the Earth and Planetary Interiors*, 265, 43-53.
- Sokol, A. G., Tomilenko, A. A., Bul'bak, T. A., Kruk, A. N., Zaikin, P. A., Sokol, I. A., Seryotkin, Y. V., Palyanov, Y. N. (2018). The Fe-C-O-H-N system at 6.3–7.8 GPa and 1200–1400° C: implications for deep carbon and nitrogen cycles. *Contributions to Mineralogy and Petrology*, 173(6), 1-17.
- Sokol, A.G., Khokhryakov, A.F., Borzdov, Y., Kupriyanov, I.N., Palyanov, Y.N., 2019. Solubility of carbon and nitrogen in a sulfur-bearing iron melt: Constraints for siderophile behavior at upper mantle conditions. *American Mineralogist* 104, 1857-1865.
- Stachel, T., Harris, J.W., Brey, G.P., 1998. Rare and unusual mineral inclusions in diamonds from Mwadui, Tanzania. *Contribution to Mineralogy and Petrology* 132, 34-47.
- Stachel, T., Harris, J.W., Muehlenbachs, K. 2009. Sources of carbon in inclusions bearing diamonds. *Lithos* 112, 625-637.
- Stachel, T., Chacko, T., Luth, R.W., 2017. Carbon isotope fractionation during diamond growth in depleted peridotite: Counterintuitive insights from modelling water-maximum CHO fluids as multi-component systems. *Earth and Planetary Science Letters* 473, 44-51.
- Stout, V.L., Gibon M.D., 1955. Gettering of gas by titanium. *Journal of Applied Physics* 26, 1488-1492.

- Sun, Q., 2009. The Raman OH stretching bands of liquid water. *Vibrational Spectroscopy* 51, 213-217.
- Thomassot, E., Cartigny, P., Harris, J.W., Viljoen, K.S., 2007. Methane-related diamond crystallization in the Earth's mantle: stable isotope evidence from a single diamond-bearing xenolith. *Earth and Planetary Science Letters* 257, 362-371.
- Toby, B.H., 2001. EXPGUI, a graphical user interface for GSAS. *Journal of Applied Crystallography* 34, 210-213.
- Tschauner, O., Huang, S., Greenberg, E., Prakapenka, V.B., Ma, C., Rossman, G.R., Shen, A.H., Zhang, D., Newville, M., Lanzirotti, A., Tait, K., 2018. Ice-VII inclusions in diamonds: Evidence for aqueous fluid in Earth's deep mantle. *Science* 359, 1136-1139.
- Viljoen K.S., Dobbe, R., Smit, B., Thomassot E., Cartigny P., 2004. Petrology and geochemistry of a diamondiferous lherzolite from the Premier diamond mine, South Africa. *Lithos* 77, 539-552.
- Weiss, Y. Kiflawi, I., Davies, N., Navon, O. 2014. High-density fluids and the growth of monocrystalline diamonds. *Geochimica et Cosmochimica Acta* 141, 145-159